Supplemental Material for "Helical Topological Superconducting Pairing at Finite Excitation Energies"

Masoud Bahari,[1,2,*] Song-Bo Zhang,[3,4] Chang-An Li,[1,2] Sang-Jun Choi,[5] Philipp Rüßmann,[1,6] Carsten Timm,[2,7] and Björn Trauzettel[1,2]

[1] *Institute for Theoretical Physics and Astrophysics, University of Würzburg, D-97074 Würzburg, Germany*
[2] *Würzburg-Dresden Cluster of Excellence ct.qmat, Germany*
[3] *Hefei National Laboratory, Hefei, Anhui, 230088, China*
[4] *International Center for Quantum Design of Functional Materials (ICQD), University of Science and Technology of China, Hefei, Anhui, 230026, China*
[5] *Department of Physics Education, Kongju National University, Gongju 32588, Republic of Korea*
[6] *Peter Grünberg Institut, Forschungszentrum Jülich and JARA, D-52425 Jülich, Germany*
[7] *Institute of Theoretical Physics, Technische Universität Dresden, 01062 Dresden, Germany*

(Dated: May 31, 2024)

In this supplemental material, we explain why topological phase transitions (TPTs) at finite energies (FEs) only occur in odd-parity pairing channels. In Sec. II, we show the constraints imposed by rotational symmetry in pseudospin space on the FE pairing potential. We present the $j = 3/2$ matrix formalism of global symmetry operators in the BdG formalism given in Sec. III. Due to the inversion symmetry, we propose an alternative method to capture the topological index of the system in terms of negative parity of the eigenstates away from the Fermi energy. In Sec. IV, we explore the constraints imposed on both the normal state and pairing channels through the interplay of crystalline symmetry and time-reversal symmetry. Such analysis reveals the connection between rotational operations in pseudospin space and the combined influence of crystalline symmetry and time-reversal symmetry. Next, we discuss the stability of helical topological surface states at finite excitation energies under randomness of chemical potential and magnetization given in Sec. V. Additionally, the analytical approach for the derivation of the helical Dirac points at the surface and the effective 2D helical surface Hamiltonian away from the Fermi energy are described in detail in Sec. VI and Sec. VII, respectively. Moreover, we analyze the value for the interband pairing in weakly hole-doped YPdBi using a combination of $\mathbf{k}\cdot\mathbf{p}$ and density functional theory calculations, see Sec. VIII. In the last section, we obtain the explicit form of cubic pairing matrices.

CONTENTS

I. TOPOLOGICAL PHASE TRANSITIONS AT FINITE ENERGIES

In this section, we address why TPTs at FEs occur only in odd-parity multiband superconductors with time-reversal symmetry. We show that the FE pairing potential is odd under the parity operation. To this end, we start by examining the parity and time-reversal symmetry properties of the normal state and the pairing potential. A fermionic state $|\mathbf{k}, m_j\rangle$, with $\mathbf{k}$ as the 3D momentum, and m_j being the magnetic quantum number of total angular momentum j, transforms under inversion P and time-reversal T operations, respectively, as

$$P|\mathbf{k}, m_j\rangle = |-\mathbf{k}, m_j\rangle, \tag{1}$$
$$T|\mathbf{k}, m_j\rangle = (-1)^{j+m_j}|-\mathbf{k}, -m_j\rangle. \tag{2}$$

Inversion symmetry acts only on the momenta and the magnetic quantum number remains intact. In this case, the matrix form of the inversion operator is a 4×4 identity matrix. The matrix representation of the anti-unitary time-reversal operator takes the form $\hat{T} = \hat{\mathcal{R}}\mathcal{K}$ with $\mathcal{K}$ being the complex conjugation and the unitary part $\hat{\mathcal{R}} = e^{i\pi\hat{J}_y} = i\hat{\sigma}_x \otimes \hat{\sigma}_y$.

The normal state preserves inversion and time-reversal

symmetries described by

$$\hat{P}\hat{\mathcal{H}}_{\mathbf{k}}\hat{P}^{-1}=\hat{\mathcal{H}}_{-\mathbf{k}},\quad \hat{\mathcal{R}}\hat{\mathcal{H}}^{*}_{\mathbf{k}}\hat{\mathcal{R}}^{-1}=\hat{\mathcal{H}}_{-\mathbf{k}}. \tag{3}$$

Moreover, the normal state preserves the combination of these symmetries given by $(\hat{P}\hat{T})\hat{\mathcal{H}}_{\mathbf{k}}(\hat{P}\hat{T})^{-1}=\hat{\mathcal{H}}_{\mathbf{k}}$ leading to doubly degenerate eigenstates.

The parity of a pairing potential is distinguished by the orbital angular momentum of Cooper pairing, i.e., $L=2n+1$ ($L=2n$) denotes odd- (even-) parity angular momenta with n being non-negative integers. In this case, the pairing potential is odd u (even g) under the parity operation given by

$$\hat{P}\hat{\Delta}_{\mathbf{k}}\hat{P}^{-1}=-(+)\hat{\Delta}_{-\mathbf{k}}. \tag{4}$$

We can show that the BdG Hamiltonian, given in Eq. (1) of the main paper, satisfies inversion symmetry for odd- (even-) parity pairing potential given by

$$\hat{\mathcal{P}}_{u,g}\hat{H}(\mathbf{k})\hat{\mathcal{P}}^{-1}_{u,g}=\hat{H}(-\mathbf{k}), \tag{5}$$

where $\hat{\mathcal{P}}_u=\hat{\sigma}_z\otimes\hat{P}$ and $\hat{\mathcal{P}}_g=\hat{\sigma}_0\otimes\hat{P}$. Furthermore, a pairing potential is time-reversal symmetric described by

$$\hat{\mathcal{R}}\hat{\Delta}^{*}_{\mathbf{k}}\hat{\mathcal{R}}^{-1}=\hat{\Delta}_{-\mathbf{k}}=\pm\hat{\Delta}_{\mathbf{k}}, \tag{6}$$

where $-(+)$ corresponds to odd- (even-) parity pairing potentials. In our investigations, we focus on odd-parity pairing potentials which preserve time-reversal symmetry.

Due to inversion symmetry in the normal state, the pseudospin operator $\hat{V}_{\mathbf{k}}=\{\hat{V}^{+}_{\mathbf{k}},\hat{V}^{-}_{\mathbf{k}}\}$ is an even-parity matrix function, i.e., $\hat{V}^{\pm}_{\mathbf{k}}=\hat{V}^{\pm}_{-\mathbf{k}}$. It is given explicitly by

$$\hat{V}^{+}_{\mathbf{k}}=\frac{1}{2}\frac{|\mathbf{k}_{||}|}{|\mathbf{k}|}\begin{pmatrix}2k_zk_-/k_+^2 & k_-/k_+\\ \sqrt{3}k_-/k_+ & 0\\ 0 & \sqrt{3}\\ 1 & -2k_z/k_-\end{pmatrix}, \tag{7}$$

and

$$\hat{V}^{-}_{\mathbf{k}}=\frac{1}{\Gamma^{-}_{\mathbf{k}}}\begin{pmatrix}2\sqrt{3}k_zk_-\mathbf{k}^2_{||}/k_+^2 & -\sqrt{3}k_-^2\\ -(|\mathbf{k}|^2+3k_z^2)\mathbf{k}^2_{||}/k_+^2 & 0\\ 0 & |\mathbf{k}|^2+3k_z^2\\ \sqrt{3}\mathbf{k}^2_{||} & 2\sqrt{3}k_zk_+\end{pmatrix}, \tag{8}$$

where $\mathbf{k}^2_{||}=k_x^2+k_y^2$, $\Gamma^{-}_{\mathbf{k}}=2|\mathbf{k}|\sqrt{|\mathbf{k}|^2+3k_z^2}$, $|\mathbf{k}|=\sqrt{\mathbf{k}^2_{||}+k_z^2}$, and $k_\pm=k_x\pm ik_y$.

The parity of the pairing potential projected onto the pseudospin basis, i.e., $\hat{\Delta}^{\nu\nu'}_{\mathbf{k}}$ with $\nu\nu'\in\{+,-\}$, is the same as the parity of the unprojected pairing potential. We prove this by the symmetry relation

$$\begin{aligned}\hat{\mathfrak{P}}\hat{\Delta}^{\nu\nu'}_{\mathbf{k}}\hat{\mathfrak{P}}^{-1}&=\hat{\mathfrak{P}}\hat{V}^{\nu\dagger}_{\mathbf{k}}\hat{\Delta}_{\mathbf{k}}(\hat{V}^{\nu'\dagger}_{-\mathbf{k}})^{T}\hat{\mathfrak{P}}^{-1}\\ &=\hat{\mathfrak{P}}\hat{V}^{\nu\dagger}_{\mathbf{k}}(\pm\hat{P}^{-1}\hat{\Delta}_{-\mathbf{k}}\hat{P})(\hat{V}^{\nu'\dagger}_{-\mathbf{k}})^{T}\hat{\mathfrak{P}}^{-1}\\ &=\pm\hat{V}^{\nu\dagger}_{-\mathbf{k}}\hat{\Delta}_{-\mathbf{k}}(\hat{V}^{\nu'\dagger}_{+\mathbf{k}})^{T}\\ &=\pm\hat{V}^{\nu\dagger}_{\mathbf{k}}\hat{\Delta}_{-\mathbf{k}}(\hat{V}^{\nu'\dagger}_{-\mathbf{k}})^{T}\\ &=\pm\hat{\Delta}^{\nu\nu'}_{-\mathbf{k}},\end{aligned} \tag{9}$$

where $\hat{\mathfrak{P}}$ is the inversion operator defined by a 2×2 identity matrix in pseudospin basis. Note that to derive Eq. (9), we consider the even-parity property of the eigenspinors. This shows that the inversion symmetry of the normal state is crucial to the determine the parity of the projected pairing. Therefore, the FE pairing potential, which is responsible for TPTs at FEs, has odd- (even-) parity if the orbital angular momentum of Cooper pairing is odd (even), i.e.,

$$\hat{\mathfrak{P}}\hat{\Delta}^{+-}_{\mathbf{k}}\hat{\mathfrak{P}}^{-1}=-(+)\hat{\Delta}^{+-}_{-\mathbf{k}}. \tag{10}$$

In the lattice representation, we replace even (odd) momenta in the finite energy pairing potential $\hat{\Delta}^{+-}_{k_\nu}$ by

$$k_\nu^{2n+1}\to[2(1-\cos(k_\nu))]^n\sin(k_\nu),\quad \text{for } L=\text{odd}, \tag{11}$$

$$k_\nu^{2n}\to[2(1-\cos(k_\nu))]^n,\quad \text{for } L=\text{even}, \tag{12}$$

where $\nu\in\{x,y,z\}$ and we assume the lattice constant to be unity. The odd-parity pairing channels contain odd powers of momenta in $\hat{\Delta}^{+-}_{\mathbf{k}}$ along the TPTs direction. Thus, the $\sin(k_\nu)$ term in Eq. (11) forces $\hat{\Delta}^{+-}_{k_\nu=\pm\pi}=0$ at the parity-time-reversal-invariant momenta (PTRIM), i. e., $k_\nu=\pm\pi$. This allows to close and reopen the gap, through the manipulation of the normal state parameters at FEs. Therefore, helical Dirac surface states emerge only for the odd-parity pairing channels.

In contrast, bulk bands for even-parity pairing channels at FEs never close at $k_\nu=\pm\pi$, i.e., $\hat{\Delta}^{+-}_{k_\nu=\pm\pi}=4^n\neq0$. This prohibits the quantization of the topological index. Therefore, the system remains in the topologically trivial phase.

We illustrate the aforementioned general argument by two examples. Since we focus on the p-wave pairing channel, the momenta appear in linear order, i.e., $L=1$ ($n=0$). Consider the A_{2u} pairing along the direction $\mathbf{k}=(0,0,k_z)$. The BdG Hamiltonian is block diagonal through the unitary transformation constructed from $\hat{\mathcal{D}}_{\mathbf{n}}(\pi,\epsilon)$ symmetry in the interband basis, i.e., $\hat{\mathscr{H}}''(0,0,k_z)=\text{diag}(\hat{h}^{-+}_{k_z,+},\hat{h}^{+-}_{k_z,+},\hat{h}^{+-}_{k_z,-},\hat{h}^{-+}_{k_z,-})$. The explicit matrix form of $\hat{h}^{+-}_{k_z,\pm}$ in the lattice representation is

$$\hat{h}^{+-}_{k_z,\pm}=\begin{pmatrix}-E^{-}_{k_z} & \Delta\sin(k_z)\\ \Delta\sin(k_z) & E^{+}_{k_z}\end{pmatrix}, \tag{13}$$

where the off-diagonal terms correspond to the FE pairing. In Eq. (13), $-E^-_{k_z}$ ($E^+_{k_z}$) is the hole (electron) band given by

$$E^-_{k_z} = 2(\alpha + \beta/4)(1 - \cos(k_z)) - \mu, \quad (14)$$

$$E^+_{k_z} = 2(\alpha + 9\beta/4)(1 - \cos(k_z)) - \mu. \quad (15)$$

The TPT occurs at the PTRIM $\mathbf{k} = (0, 0, \pm\pi)$ where the spectrum of Eq. (13) becomes

$$\varepsilon_1 = \mu - (4\alpha + \beta), \quad \varepsilon_2 = 4\alpha + 9\beta - \mu. \quad (16)$$

We assume the normal state energy bands to have identical sign of curvature, i.e., $\mathrm{sgn}(\alpha) = \mathrm{sgn}(\beta) = \pm 1$. In this case, the system exhibits a gap at $\mathbf{k} = (0, 0, \pm\pi)$, i.e., $|\varepsilon_1 - \varepsilon_2| = 2|4a + 5b - \mu| > 0$. The TPT occurs when $|\varepsilon_1 - \varepsilon_2| = 0$. This results in the phase transition relation $\mu = 4\alpha + 5\beta$. Hence, the TPT at nonzero excitation energies can occur through the interplay between odd-parity superconductivity and normal state crossings at finite excitation energies.

In realistic materials, α and β are fixed and the system can exhibit a topological phase for a certain range of chemical potentials. This is illustrated by the topological phase diagram in Fig. 1(c) in the main text.

In contrast, the FE pairing never vanishes at PTRIM for even-parity pairing channels. To illustrate this, consider the even-parity s-wave E_g pairing given by the pairing matrix $\hat{\Delta}_{\mathbf{k}} = (\Delta/3)(2\hat{J}_z^2 - \hat{J}_x^2 - \hat{J}_y^2)\hat{\mathcal{R}}$ [1]. This pairing matrix exhibits vanishing (nonvanishing) intra- (inter-) band pairing at momenta $2k_z^2 = k_x^2 + k_y^2$, i.e., $\hat{\Delta}^{\mathrm{intra}}_{\mathbf{k}} = 0$ and $\hat{\Delta}^{+-}_{\mathbf{k}} \neq 0$. Therefore, this instability channel is a candidate for the TPTs at FEs. The FE pairing is even under the parity exchange, i.e., $\hat{\mathfrak{P}}\hat{\Delta}^{+-}_{\mathbf{k}}\hat{\mathfrak{P}}^{-1} = \hat{\Delta}^{+-}_{-\mathbf{k}}$ with $\hat{\Delta}^{+-}_{\mathbf{k}} = \Delta(k_+/k_-)\hat{\tau}_x$ where $k_\pm = k_x \pm ik_y$. In this case, the interband superconducting Hamiltonian becomes

$$\hat{\mathsf{H}}^{+-}_{\mathbf{k}} = \begin{pmatrix} E^+_{\mathbf{k}}\hat{\tau}_0 & \Delta(k_+/k_-)\hat{\tau}_x \\ \Delta(k_-/k_+)\hat{\tau}_x & -E^-_{\mathbf{k}}\hat{\tau}_0 \end{pmatrix}, \quad (17)$$

where

$$E^+_{\mathbf{k}} = (3/8)(4\alpha + 9\beta)(k_x^2 + k_y^2) - \mu, \quad (18)$$

$$E^-_{\mathbf{k}} = (3/8)(4\alpha + \beta)(k_x^2 + k_y^2) - \mu. \quad (19)$$

Equation (17) preserves a rotational symmetry along the z-axis in pseudospin basis with rotation angle $\theta = \pi$ given by $\hat{\mathcal{D}}_{\mathbf{n}_z}(\pi, 1) = \mathrm{diag}(i\hat{\tau}_z, -i\hat{\tau}_z)$. Therefore, $\hat{\mathsf{H}}^{+-}_{\mathbf{k}}$ becomes diagonal in the eigenbasis of $\hat{\mathcal{D}}_{\mathbf{n}_z}(\pi, 1)$ labeled by eigenvalues $\lambda = \pm i$ obtained by $\hat{\mathcal{U}}^\dagger\hat{\mathsf{H}}^{+-}_{\mathbf{k}}\hat{\mathcal{U}} = \mathrm{diag}(\hat{h}^{+-}_{\mathbf{k},+i}, \hat{h}^{+-}_{\mathbf{k},-i})$ with

$$\hat{h}^{+-}_{\mathbf{k},\pm i} = \begin{pmatrix} -E^-_{\mathbf{k}} & \Delta(k_-/k_+) \\ \Delta(k_+/k_-) & E^+_{\mathbf{k}} \end{pmatrix}, \quad (20)$$

where the matrix of eigenvectors for $\hat{\mathcal{D}}_{\mathbf{n}_z}(\pi, 1)$ is given by

$$\hat{\mathcal{U}} = \begin{pmatrix} 0 & 1 & 0 & 0 \\ 0 & 0 & 0 & 1 \\ 0 & 0 & 1 & 0 \\ 1 & 0 & 0 & 0 \end{pmatrix}. \quad (21)$$

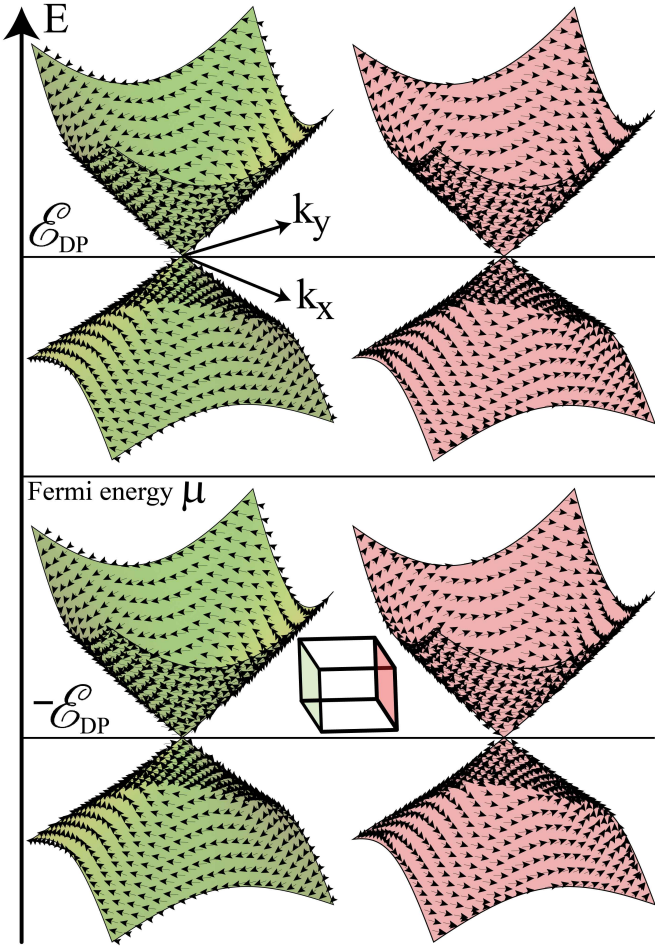

Figure 1. Helical topological Dirac cones at finite excitation energies induced by FE Cooper pairing. A pair of helical Dirac cones (pink) emerge on a surface and the degenerate partner appears on the other surface (green). Black arrows illustrate the spin texture of the surface states exhibiting spin-momentum locking due to the helical property. $\mathscr{E}_{\mathrm{DP}}$ denotes energy of the Dirac points and μ is the Fermi energy of the normal state.

The spectrum of Eq. (20) is always gapped at FEs. Hence, TPTs at FEs are not possible.

II. PSEUDOSPIN ROTATION SYMMETRY PROPERTIES

In this section, we explain the constraint imposed by pseudospin rotation symmetry on the FE pairing potential. The motivation behind such analysis is to show the explicit form of a general FE pairing matrix fulfilling the pseudospin rotation symmetry. To this end, we present the FE pairing matrix in a general form

$$\hat{\Delta}^{+-}_{\mathbf{k}} \equiv \mathfrak{g}_{\mathbf{k}} \cdot \hat{\boldsymbol{\tau}}, \quad (22)$$

where the four-component $\mathfrak{g}_{\mathbf{k}}$ vector is given by $\mathfrak{g}_{\mathbf{k}} = (\mathfrak{g}_0, \mathfrak{g}_x, \mathfrak{g}_y, \mathfrak{g}_z)$ with the components being momentum de-

pendent functions (this dependency is dropped). The four-component vector of Pauli matrices is defined in the interband basis by $\hat{\boldsymbol{\tau}} = (\hat{\tau}_0, \hat{\tau}_x, \hat{\tau}_y, \hat{\tau}_z)$ with $\hat{\tau}_0$ being a 2×2 identity matrix.

The matrix representation of FE pairing potential converts to a pairing function $\delta^{+-}_{\mathbf{k},\lambda}$ (see Eq. (5) in the main text) in the presence of $\hat{\mathcal{D}}_{\mathbf{n}}(\pi,\epsilon)$ symmetry where the rotation angle is about the arbitrary unit vector $\mathbf{n} = (n_x, n_y, n_z)$. In this case, the relation between $\hat{\Delta}^{+-}_{\mathbf{k}}$ and $\delta^{+-}_{\mathbf{k},\lambda}$ can be distinguished by the components of the vector $\mathfrak{g}_{\mathbf{k}}$. Interestingly, the pseudospin rotation symmetry about the x(y)[z] axis, defined by

$$\mathbf{n}_x \equiv (1,0,0),\ \mathbf{n}_y \equiv (0,1,0),\ \mathbf{n}_z \equiv (0,0,1), \tag{23}$$

enforces $\delta^{+-}_{\mathbf{k},\lambda}$ to select up to two components of the vector $\mathfrak{g}_{\mathbf{k}}$. After some algebra, such constraints for the $\epsilon=-1$ representation can be obtained by

$$[\hat{\mathcal{D}}_{\mathbf{n}_z}(\pi,-1), \hat{\mathsf{H}}^{+-}_{\mathbf{k}}]=0 \rightarrow \delta^{+-}_{\mathbf{k},\lambda} = \mathfrak{g}_0 + \lambda\mathfrak{g}_z, \tag{24}$$
$$[\hat{\mathcal{D}}_{\mathbf{n}_y}(\pi,-1), \hat{\mathsf{H}}^{+-}_{\mathbf{k}}]=0 \rightarrow \delta^{+-}_{\mathbf{k},\lambda} = \lambda i\mathfrak{g}_x - \mathfrak{g}_z, \tag{25}$$
$$[\hat{\mathcal{D}}_{\mathbf{n}_x}(\pi,-1), \hat{\mathsf{H}}^{+-}_{\mathbf{k}}]=0 \rightarrow \delta^{+-}_{\mathbf{k},\lambda} = \mathfrak{g}_0 + \lambda\mathfrak{g}_x. \tag{26}$$

To interpret the above relations, we consider Eq. (24) as an example. In this case, $\delta^{+-}_{\mathbf{k},\lambda}$ preserves the pseudospin rotation symmetry under the rotation angle $\theta=\pi$ about the z-axis if either $\mathfrak{g}_0$ or $\mathfrak{g}_z$, or both of them are finite, and the other components vanish, i.e., $\mathfrak{g}_{\mathbf{k}} = (\mathfrak{g}_0, 0, 0, \mathfrak{g}_z)$. This is a useful result since we can directly ascertain the pseudospin rotation symmetry of a FE pairing potential in multiband superconductors by checking only the components of the vector $\mathfrak{g}_{\mathbf{k}}$.

The dot product of the vector $\mathfrak{g}_{\mathbf{k}}$ and the Pauli matrices in Eq. (22) allows us to find the relation between $\hat{\Delta}^{+-}_{\mathbf{k}}$ and a proper $\hat{\mathcal{D}}_{\mathbf{n}}(\pi,\epsilon)$ symmetry given by

$$\hat{\mathcal{D}}_{\mathbf{n}_z}(\pi,-1) : \hat{\Delta}^{+-}_{\mathbf{k}} = \mathfrak{g}_0\hat{\tau}_0 + \mathfrak{g}_z\hat{\tau}_z, \tag{27}$$
$$\hat{\mathcal{D}}_{\mathbf{n}_y}(\pi,-1) : \hat{\Delta}^{+-}_{\mathbf{k}} = \mathfrak{g}_x\hat{\tau}_x + \mathfrak{g}_z\hat{\tau}_z, \tag{28}$$
$$\hat{\mathcal{D}}_{\mathbf{n}_x}(\pi,-1) : \hat{\Delta}^{+-}_{\mathbf{k}} = \mathfrak{g}_0\hat{\tau}_0 + \mathfrak{g}_x\hat{\tau}_x. \tag{29}$$

Importantly, we observe that the component $\mathfrak{g}_y$ in Eqs. (24-29) is absent. However, the pseudospin rotation symmetry with $\epsilon=+1$ representation reveals the allowed symmetry form of $\delta^{+-}_{\mathbf{k},\lambda}$ including the y-component of $\mathfrak{g}_{\mathbf{k}}$,

$$[\hat{\mathcal{D}}_{\mathbf{n}_z}(\pi,1), \hat{\mathsf{H}}^{+-}_{\mathbf{k}}]=0 \rightarrow \delta^{+-}_{\mathbf{k},\lambda} = \mathfrak{g}_x - i\lambda\mathfrak{g}_y, \tag{30}$$
$$[\hat{\mathcal{D}}_{\mathbf{n}_y}(\pi,1), \hat{\mathsf{H}}^{+-}_{\mathbf{k}}]=0 \rightarrow \delta^{+-}_{\mathbf{k},\lambda} = \mathfrak{g}_0 + \lambda\mathfrak{g}_y, \tag{31}$$
$$[\hat{\mathcal{D}}_{\mathbf{n}_x}(\pi,1), \hat{\mathsf{H}}^{+-}_{\mathbf{k}}]=0 \rightarrow \delta^{+-}_{\mathbf{k},\lambda} = -i\lambda\mathfrak{g}_y - \mathfrak{g}_z. \tag{32}$$

In this case, the $\hat{\mathcal{D}}_{\mathbf{n}}(\pi,\epsilon)$ symmetry forces the FE pairing matrix to have the explicit form

$$\hat{\mathcal{D}}_{\mathbf{n}_z}(\pi,1) : \ \hat{\Delta}^{+-}_{\mathbf{k}} = \mathfrak{g}_x\hat{\tau}_x + \mathfrak{g}_y\hat{\tau}_y, \tag{33}$$
$$\hat{\mathcal{D}}_{\mathbf{n}_y}(\pi,1) : \ \hat{\Delta}^{+-}_{\mathbf{k}} = \mathfrak{g}_0\hat{\tau}_0 + \mathfrak{g}_y\hat{\tau}_y, \tag{34}$$
$$\hat{\mathcal{D}}_{\mathbf{n}_x}(\pi,1) : \ \hat{\Delta}^{+-}_{\mathbf{k}} = \mathfrak{g}_y\hat{\tau}_y + \mathfrak{g}_z\hat{\tau}_z. \tag{35}$$

Taking into account Eqs. (27-29) and (33-35), we can understand the explicit form of the $\hat{\mathcal{D}}_{\mathbf{n}}(\pi,\epsilon)$ symmetry along the TPT direction by looking at the components of $\hat{\Delta}^{+-}_{\mathbf{k}}$, e.g., the last column of Table. I in the main text. For instance, one of the TPT directions for the T_{2u} irrep is $\mathbf{k}\in(\pm k, 0, \pm k)$ and the FE pairing potential is given by $\hat{\Delta}^{+-}_{k} = \Delta k(\pm\hat{\tau}_0/3 - i\hat{\tau}_y)$. According to Eq. (34), $\hat{\Delta}^{+-}_{k}$ preserves $\hat{\mathcal{D}}_{\mathbf{n}_y}(\pi,1)$ symmetry with $\mathfrak{g}_0 = \pm\Delta k/3$ and $\mathfrak{g}_y = \pm i\Delta k$.

Note that when $\hat{\Delta}^{+-}_{\mathbf{k}}$ contains only one component of $\mathfrak{g}_{\mathbf{k}}$ along the TPT direction, the rotation axis of the $\hat{\mathcal{D}}_{\mathbf{n}}(\pi,\epsilon)$ is not unique. Importantly, the momentum dependency of components of the $\mathfrak{g}_{\mathbf{k}}$ along the TPT direction is proportional to the orbital angular momentum of Cooper pairing. For instance, $\mathfrak{g}_{\mathbf{k}}$ is proportional to linear order of momenta at TPT directions since we focus on p-wave pairing, i, e., $L=1$.

The reason for having two representations for the $\hat{\mathcal{D}}_{\mathbf{n}}(\pi,\epsilon)$ symmetry can be seen by the unitary transformation $\hat{\mathcal{V}}$ between the eigenbases for $\epsilon=+1$ and $\epsilon=-1$,

$$\hat{\phi}_{+1} = \hat{\mathcal{V}}\hat{\phi}_{-1}, \quad \hat{\mathcal{V}} = \hat{\mathcal{V}}^{-1} = \hat{\mathcal{V}}^{\dagger} = \begin{pmatrix} 0 & 0 & 1 & 0 \\ 0 & 1 & 0 & 0 \\ 1 & 0 & 0 & 0 \\ 0 & 0 & 0 & 1 \end{pmatrix}, \tag{36}$$

where $\hat{\phi}_{\epsilon=\pm1} = \hat{\mathcal{U}}^{-1}\hat{\varphi}^{+-}_{\mathbf{k}}$ with $\hat{\varphi}^{+-}_{\mathbf{k}}$being the 4×1 column as the basis of FE superconducting Hamiltonian $\hat{\mathsf{H}}^{+-}_{\mathbf{k}}$, and $\hat{\mathcal{U}}$ is the eigenvector matrix for $\hat{\mathcal{D}}_{\mathbf{n}}(\pi,\epsilon)$ operator.

III. GLOBAL SYMMETRIES

The explicit matrix representations for time-reversal and particle-hole symmetry operators in BdG formalism are given by $\hat{\mathcal{T}} = i\hat{\varsigma}_0\otimes\hat{\sigma}_x\otimes\hat{\sigma}_y\mathcal{K}$ and $\hat{\mathscr{P}} = \hat{\varsigma}_x\otimes\hat{\sigma}_0\otimes\hat{\sigma}_0\mathcal{K}$, respectively. Here, $\mathcal{K}$ is the complex-conjugate operator, $\hat{\varsigma}_i$ and $\hat{\sigma}_i$ with $i\in\{0,x,y,z\}$ are Pauli matrices acting on particle-hole and spin subspaces, respectively. The symmetry relation reads $\hat{\mathcal{O}}\hat{H}^*(\mathbf{k})\hat{\mathcal{O}}^{-1} = \epsilon\hat{H}(-\mathbf{k})$ with $\epsilon=+1(-1)$ for $\hat{\mathcal{O}} = \hat{\mathcal{T}}(\hat{\mathscr{P}})$. Additionally, we can construct a chiral symmetry operator $\hat{\mathcal{C}} = \hat{\mathcal{T}}\hat{\mathscr{P}}$ fulfilling $\hat{\mathcal{C}}\hat{H}(\mathbf{k})\hat{\mathcal{C}}^{-1} = -\hat{H}(\mathbf{k})$ [2–4]. The symmetry operators have the properties $\hat{\mathcal{T}}^2 = -1$ and $\hat{\mathscr{P}}^2 = 1$. In addition, the inversion symmetry operator is defined by $\hat{\mathcal{P}}_u = \hat{\sigma}_z\otimes\hat{P}$ fulfilling $\hat{\mathcal{P}}_u^2 = 1$.

We complete our discussion on topological phase transitions induced by FE pairing by proposing an alternative approach to calculate the topological index due to the presence of inversion symmetry [5, 6]. The BdG Hamiltonian commutes with $\hat{\mathcal{P}}_u$ and $\hat{T}$ operators at eight PTRIM given by

$$\mathbf{k}_{\mathrm{p}}=(0,0,0), \mathbf{k}_{\mathrm{p}}=(0,0,\pi), \mathbf{k}_{\mathrm{p}}=(0,\pi,0), \mathbf{k}_{\mathrm{p}}=(\pi,0,0),$$
$$\mathbf{k}_{\mathrm{p}}=(0,\pi,\pi), \mathbf{k}_{\mathrm{p}}=(\pi,\pi,0), \mathbf{k}_{\mathrm{p}}=(\pi,0,\pi), \mathbf{k}_{\mathrm{p}}=(\pi,\pi,\pi). \tag{37}$$

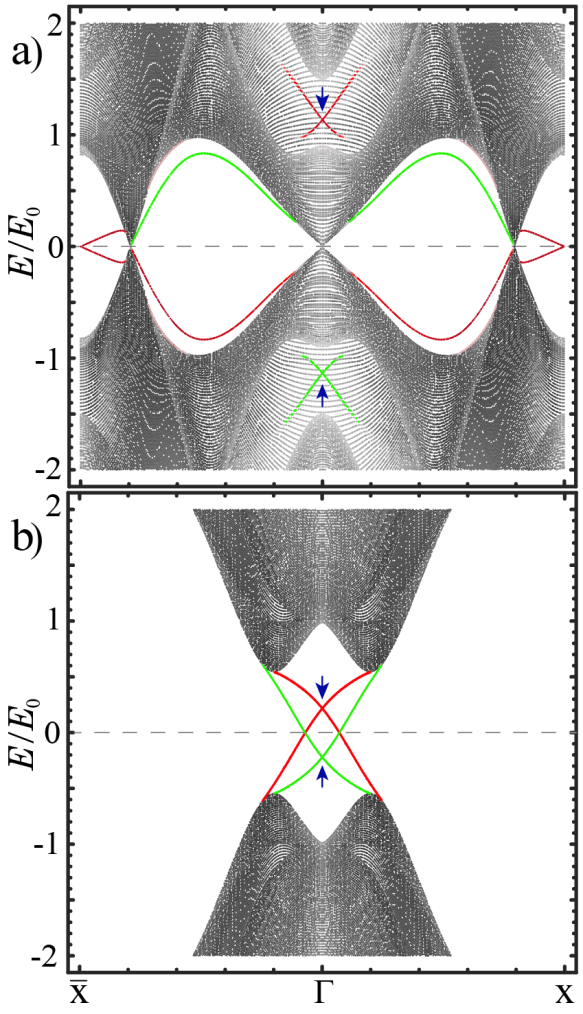

Figure 2. Enlarged view of the spectra given in Fig. 2(c) of the main text. The thickness is 180 layers and $E_0 = \Delta/2$. The high-symmetry points are $X = (0, \pi/a, 0)$ and $\Gamma = (0, 0, 0)$ where a is the lattice constant in tight binding calculations. The surface (bulk) states are colorful (dark). Blue arrows indicate the helical Dirac points induced by topological FE pairing. The gray dashed line indicates the Fermi energy. (a) [(b)] Surface states inside (outside) of the bulk states before (after) a Lifshitz transition for $\mu = -5.2E_0$ ($\mu = -E_0$). (b) The helical surface states resemble a butterfly shape, and establish dispersive Majorana modes away from the high symmetry points at the Fermi energy. The other parameters are $\alpha = -\Delta/2$ and $\beta = 0.3\alpha$.

Generally, the FE pairing arising form odd-parity pairing channels can induce topological phase transition along the directions $\mathbf{K}$ connecting the PTRIM. The criteria rely on the presence and absence of finite and low energy pairings along such directions, respectively. In this case, the BdG Hamiltonian becomes block diagonal

$$\hat{\mathscr{H}}'(\mathbf{K}) = \mathrm{diag}\big(\hat{h}^{+-}_{\mathbf{K},+}, \hat{h}^{+-}_{\mathbf{K},+}, \hat{h}^{-+}_{\mathbf{K},-}, \hat{h}^{-+}_{\mathbf{K},-}\big), \tag{38}$$

	$\hat{\mathcal{T}}$	$\hat{\mathscr{P}}$	$\hat{\mathcal{C}}$	$\hat{\mathcal{P}}_u$
$\hat{\mathcal{T}}$	Commute	Commute	Commute	Commute
$\hat{\mathscr{P}}$		Commute	Commute	Anticommute
$\hat{\mathcal{C}}$			Commute	Anticommute
$\hat{\mathcal{P}}_u$				Commute

Table I. Commutation/anticommutation relations between the discrete symmetries.

where

$$\hat{h}^{+-}_{\mathbf{K},\lambda} = \begin{pmatrix} -E^{-}_{\mathbf{K}} & \left(\delta^{+-}_{\mathbf{K},\lambda}\right)^{*} \\ \delta^{+-}_{\mathbf{K},\lambda} & E^{+}_{\mathbf{K}} \end{pmatrix}. \tag{39}$$

In Eq. (38), $\hat{h}^{-+}_{\mathbf{K},\lambda}$ is the particle-hole partner of $\hat{h}^{+-}_{\mathbf{K},\lambda}$ implied by $\hat{\tau}_y(\hat{h}^{+-}_{\mathbf{K},\lambda})^*\hat{\tau}_y^{-1} = \hat{h}^{-+}_{\mathbf{K},\lambda}$. Note that each block $\hat{h}^{\pm\mp}_{\mathbf{k},\lambda}$ preserves an effective time-reversal symmetry $\hat{T} = \mathcal{K}$ with $\hat{T}^2 = +1$. Particle-hole symmetry and the conventional time-reversal symmetry with $\hat{T}^2 = -1$ are broken due to the different diagonal entries in the symmetry blocks. Also, each block in Eq. (38) satisfies inversion symmetry implied by $\hat{\tau}_z\hat{h}^{\nu\nu'}_{\mathbf{K},\lambda}\hat{\tau}_z^{-1} = \hat{h}^{\nu\nu'}_{-\mathbf{K},\lambda}$ with $\nu, \nu' \in \{+, -\}$. In this case, $\hat{h}^{\nu\nu'}_{\mathbf{K},\lambda}$ commutes with $\hat{\tau}_z$, and the negative parity of the eigenstates associated to the lower energy band in sector $\hat{h}^{\nu\nu'}_{\mathbf{K},\lambda}$ determines the topological nature of the phase transition. Note that only one of the directions connecting the PTRIM is sufficient to capture the nontrivial topological phase induced by FE Cooper pairing. Therefore, to characterize the topological phases, we define a topological index

$$\mathcal{N} = |n_\Gamma - n_{\mathbf{p}}|, \tag{40}$$

where n_Γ and $n_{\mathbf{p}}$ are the number of negative eigenvalues of the parity operator at the Γ point $\mathbf{k}_\mathrm{p}$ = (0,0,0), and other PTRIM. Note that $\mathcal{N}$ is a $\mathbb{Z}_2$ topological index taking two values, i.e., $\mathcal{N} = 1(0)$ in the topologically nontrivial (trivial) phase. The full topological index can be derived by the summation of the topological indices associated to the decoupled blocks in Eq. (38) as

$$Z = \sum_{\lambda=\pm}(\mathcal{N}^{+-}_{\lambda} + \mathcal{N}^{-+}_{\lambda}), \tag{41}$$

where $\mathcal{N}^{\nu\nu'}_{\lambda}$ corresponds to the block $\hat{h}^{\nu\nu'}_{\mathbf{K},\lambda}$. In the topologically nontrivial phase, conservation of parity leads to the quantization of the topological index and the emergence of surface states. Pseudospin rotation symmetry ensures that the surface states come in pairs establishing FE helical Dirac points. Hence, the appearance of a pair of helical surface states at positive (negative) excitation energies is signaled by $\sum_{\lambda=\pm}\mathcal{N}^{+-}_{\lambda} = 2$ ($\sum_{\lambda=\pm}\mathcal{N}^{-+}_{\lambda} = 2$). Considering two surfaces, we observe four Dirac surface states on each surface (two for positive

excitation energies and two for negative energies) due to parity-time-reversal symmetry, cf. Fig. 1.

A Lifshitz transition can move the FE helical Dirac surface states, shown in Fig. 2(a), to the low energies. In this case, the surface states establish Majorana modes at the Fermi energy, see Fig. 2(b).

Note that the point group symmetry of the normal-state Hamiltonian for any real system is lower than the O(3) symmetry of the Luttinger-Kohn Hamiltonian discussed in the main text. The Luttinger-Kohn Hamiltonian serves as a valuable approximation for energy bands close to high-symmetry points. However, the symmetry of the superconducting (BdG) Hamiltonian is relevant for our analysis. It belongs to the O_h symmetry group, as the O(3) symmetry of the normal state transforms into cubic point group symmetry due to the pairing matrices derived through irreducible representations of the cubic point group symmetry. Importantly, the pseudospin rotation symmetry mentioned above is present for multi-band system with parity-time-reversal symmetry. Its presence is independent of the O(3) symmetry of the normal state Hamiltonian. Nonetheless, we examine our predictions when the normal state is influenced by O(3) symmetry-breaking terms. To this end, we incorporate the cubic spin-orbit coupling term to the normal state Hamiltonian as

$$\hat{\mathcal{H}}(\mathbf{k}) = \alpha|\mathbf{k}|^2\hat{I}_4 + \beta\sum_i k_i^2\hat{J}_i^2 + \gamma\sum_{i\neq j} k_i k_j \hat{J}_i\hat{J}_j - \mu, \quad (42)$$

where γ parametrizes the strength of the cubic spin-orbit coupling term. This Hamiltonian refers to the O(3) symmetry-broken case in the normal state if $\gamma \neq \beta$. We adopt the tight-binding regularization of Eq. (42) in the BdG form. The spectral result within the topologically non-trivial phase is illustrated in Fig. 3. Evidently, we can also observe the emergence of helical Dirac surface states with particle-hole character away form the Fermi energy due to the unconventional finite energy Cooper pairing in the case with broken O(3) symmetry, see Fig. 3(a,b). In addition, we investigate a Lifshitz transition around the Γ point by a variation of the chemical potential as illustrated in Fig. 3(c,d). In this case, the surface states are shifted towards low energies. If the superconducting gap possesses nodes at zero excitation energy, these surface states connect the nodal points, see Fig. 3(c). If the superconducting gap is fully developed at zero excitation energy, these surface states connect to the bulk states at finite excitation energy, see Fig. 3(d).

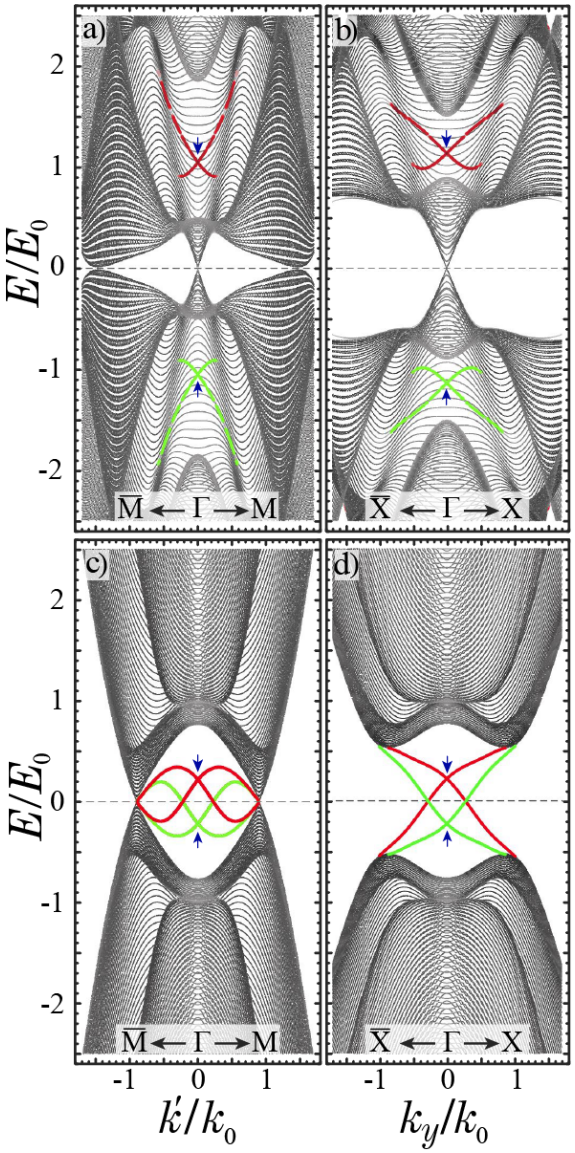

Figure 3. Spectra of a slab with (001) surfaces in the topologically nontrivial regime. The thickness is 100 layers. The cubic spin-orbit coupling term is chosen as $\gamma = \alpha$. Hence, O(3) symmetry is broken in the normal state. In panels (a) and (c), k' defines the direction in momentum space with $k_x = k_y$. The chemical potential is chosen as (a) $\mu = -5.2E_0$, (b) $\mu = -5.1E_0$, and (c,d) $\mu = -E_0$. The other parameters are $\beta = 0.3\alpha$, $\alpha = -(2/3)\Delta$, and $E_0 = (2/3)\Delta$. The high-symmetry points are $X = (0, \pi/a, 0)$ and $M = (\pi/a, \pi/a, 0)$.

IV. POINT GROUP SYMMETRY ANALYSIS

The block diagonalization of the BdG Hamiltonian is possible in directions where the pairing potential satisfies two conditions:

1. vanishing intraband pairing,
2. nonvanishing interband pairing at finite energies.

These two conditions can be fulfilled when time-reversal T symmetry combines with twofold rotation about the $\langle 110\rangle$ axis. This symmetry operator is defined by $\hat{\mathcal{C}}_T \equiv \hat{T}\hat{C}_{2,x+y}$ having the property $\hat{\mathcal{C}}_T^2 = 1$. We then use the $\hat{C}_{2,x+y}$ operator combined with inversion $\hat{P}$ symmetry (mirror reflection), denoted as $\hat{\mathcal{C}}_P \equiv \hat{P}\hat{C}_{2,x+y}$, for block

diagonalization. In addition, the double degeneracy of states at each momenta is ensured by $\hat{P}\hat{T} = e^{-i\pi}\hat{\mathcal{C}}_T\hat{\mathcal{C}}_P$. Note that $\hat{T}$, $\hat{C}_{2,x+y}$, and $\hat{P}$ commute with each other, and $\hat{\mathcal{C}}_P^2 = -1$.

In the following, we illustrate these points by group theoretical analysis. We begin by analyzing the point group symmetry of the given BdG Hamiltonian

$$\hat{H}_{\rm BdG}(\mathbf{k}) = \begin{pmatrix} \hat{\mathcal{H}}(\mathbf{k}) & \hat{\Delta}(\mathbf{k}) \\ \hat{\Delta}^\dagger(\mathbf{k}) & -\hat{\mathcal{H}}^T(-\mathbf{k}) \end{pmatrix} \tag{43}$$

where $\hat{\mathcal{H}}(\mathbf{k})$ and $\hat{\Delta}(\mathbf{k}) = \hat{D}(\mathbf{k})e^{i\pi\hat{J}_y}$ denote normal state and pairing matrix, respectively. $\hat{H}_{\rm BdG}(\mathbf{k})$ preserves the symmetry group G if its symmetry elements, denoted as $\hat{g}$, satisfy the following condition

$$\hat{\mathcal{H}}(\mathbf{k}) \longmapsto \hat{g}\hat{\mathcal{H}}(R^{-1}\mathbf{k})\hat{g}^\dagger, \quad \hat{D}(\mathbf{k}) \longmapsto \hat{g}\hat{D}(R^{-1}\mathbf{k})\hat{g}^\dagger, \tag{44}$$

where $\hat{g}$ can for instance be a q-fold rotation and R is a 3×3 orthogonal matrix implementing rotation on momentum space. Then, the point group symmetry operation for Eq. (43) takes the form

$$\hat{\mathcal{G}}\hat{H}_{\rm BdG}(R^{-1}\mathbf{k})\hat{\mathcal{G}}^{-1} = \hat{H}_{\rm BdG}(\mathbf{k}), \tag{45}$$

where $\hat{\mathcal{G}} = \mathrm{diag}(\hat{g}, \pm\hat{g}^*)$. In our system, G for the superconducting Hamiltonian is given by

$$G = U(1)\otimes\mathscr{P}\otimes T\otimes O_h, \tag{46}$$

where $U(1)$ is a global phase-rotation symmetry, $\mathscr{P}$ (T) denotes anti-unitary particle-hole (time-reversal) symmetry, and O_h is a cubic point group symmetry. O_h describes the combination of inversion symmetry P and octahedral O point group symmetry. The O group consists of $q-$fold rotations about the $\mathbf{n}$ axis labeled by $C_{q,\mathbf{n}}$. Combining P with O, this results in $q-$fold improper rotations denoted by $PC_{q,\mathbf{n}}$.

In our study, the pairing channels are odd (even) under $\hat{P}$ ($\hat{T}$) symmetries such that $\hat{M}\hat{D}(-\mathbf{k})\hat{M}^\dagger = -(+)\hat{D}(\mathbf{k})$ with $\hat{M} = \hat{P}(\hat{T})$. Moreover, $\hat{D}(\mathbf{k})$ anti-commute with $\hat{P}\hat{T}$ symmetry, i.e., $\{\hat{D}(\mathbf{k}), \hat{P}\hat{T}\} = 0$ with $\hat{T} = \exp(i\pi\hat{J}_y)\mathcal{K}$ and $\hat{P} = \hat{I}_4$, where $\mathcal{K}$ is complex conjugation. Importantly, the generators of $\hat{D}(\mathbf{k})$ in combination with $\hat{T}$ symmetry, this can impose constraints on the pairing potential. In the main text, we focus on the A_{2u} pairing channel (spin-septet). The matrix representation of $\hat{D}(\mathbf{k})$ is $\hat{D}(\mathbf{k}) = \mathbf{k}\cdot\hat{\mathbf{T}}$ where $\hat{T}_i = \{\hat{J}_i, \hat{J}_{i+1}^2 - \hat{J}_{i+2}^2\}$ with $i+1 = y$ if $i = x$, etc., cyclically. The generators for the A_{2u} channel are $\{e^{i\pi}\hat{C}_{4z}, e^{i\pi}\hat{C}_{2,z+x}\}$, where $\hat{C}_{2,z+x}$ ($\hat{C}_{4z}$) denotes two(four)fold rotation about the [1,0,1] ([0,0,1]) axis [7]. Note that $\hat{C}_{4z}$ does not constrain the pairing channel while the rotation about C_2' axis does. In this case, normal state and pairing channel transform under twofold rotation about the C_2' axis, e.g., [1,1,0] axis, such that

$$\hat{C}_{2,x+y}\hat{D}(k_y, k_x, -k_z)\hat{C}_{2,x+y}^\dagger = -\hat{D}(\mathbf{k}), \tag{47}$$

$$\hat{C}_{2,x+y}\hat{\mathcal{E}}(k_y, k_x, -k_z)\hat{C}_{2,x+y}^\dagger = \hat{\mathcal{E}}(\mathbf{k}). \tag{48}$$

Combining $\hat{T}$ with twofold rotation symmetry denoted by $\hat{\mathcal{C}}_T = \hat{T}\hat{C}_{2,x+y}$, yielding the relation

$$\hat{\mathcal{C}}_T\hat{D}(-k_y, -k_x, k_z)\hat{\mathcal{C}}_T^\dagger = -\hat{D}(\mathbf{k}), \tag{49}$$

$$\hat{\mathcal{C}}_T\hat{\mathcal{E}}(-k_y, -k_x, k_z)\hat{\mathcal{C}}_T^\dagger = \hat{\mathcal{E}}(\mathbf{k}). \tag{50}$$

In this case, $\hat{\mathcal{C}}_T$ results in vanishing (nonvanishing) intraband (interband) pairing potentials.

We prove this at two Fermi momenta $\mathbf{k}_1$ and $\mathbf{k}_2$ (due to having two energy bands), and the crossing momenta $\mathbf{k}_3$ at finite energies. Note that $\mathbf{k}_1$ ($\mathbf{k}_2$) is associated to the Fermi momentum for the $|m_j| = 3/2$ ($|m_j| = 1/2$) Fermi surface. The $|m_j| = 1/2$ Fermi surface is constrained in a similar way by $\hat{\mathcal{C}}_T$ as the $|m_j| = 3/2$ Fermi surface. This results in point nodes in both double-degenerate Fermi surfaces along the $\langle 001\rangle$ direction. We prove this through symmetry analysis in pseudospin (Kramer's partner) representation. The double-degeneracy is guaranteed by PT symmetry. In this case, the effective pairing projected onto the intraband basis at $\mathbf{k}_1$ can be represented in the pseudospin basis as

$$\hat{\Delta}_{\rm eff}^{\nu\nu}(\mathbf{k}_1) \equiv (\mathbf{d}(\mathbf{k}_1)\cdot\hat{\sigma})(i\hat{\sigma}_y), \tag{51}$$

where $\mathbf{d}(\mathbf{k}_1) = (d_x(\mathbf{k}_1), d_y(\mathbf{k}_1), d_z(\mathbf{k}_1))$, $\hat{\sigma} = (\hat{\sigma}_x, \hat{\sigma}_y, \hat{\sigma}_z)$ is the vector of Pauli matrices in intraband pseudospin basis. Note that $\hat{\Delta}_{\rm eff}^{\nu\nu}(\mathbf{k}_1)$ is represented in pseudospin triplet state due to the odd parity of $\hat{D}(\mathbf{k})$. For $\nu = +$, $\hat{\Delta}_{\rm eff}^{\nu\nu}(\mathbf{k}_1)$ describes pairing of $|m_j| = 3/2$ states at the Fermi energy. At $\mathbf{k}_1$, spin and momentum transform under $\hat{\mathcal{C}}_T$ as

$$\hat{\mathcal{C}}_T\hat{\sigma}\hat{\mathcal{C}}_T^\dagger = (-\hat{\sigma}_y, -\hat{\sigma}_x, \hat{\sigma}_z), \ R^{-1}\mathbf{k}_1 = (-k_y, -k_x, k_z). \tag{52}$$

Consequently, along the $\langle 001\rangle$ direction, the effective pairing potential becomes $\hat{\Delta}_{\rm eff}^{++}(\mathbf{k}_1) = d_z(k_z)\hat{\sigma}_z(i\hat{\sigma}_x)$ which violates the Fermi statistics unless $d_z(\mathrm{k}_z) = 0$. Consequently, this results in point nodes along z-direction (and all equivalent directions). Moreover, the same holds true for $\hat{\Delta}_{\rm eff}^{--}(\mathbf{k}_2)$. Therefore, point 1., stated at the beginning of this section, is fulfilled leading to

$$\hat{\Delta}_{\rm eff}^{++}(\mathbf{k}_1) = \hat{\Delta}_{\rm eff}^{--}(\mathbf{k}_2) = 0. \tag{53}$$

To realize point 2., stated at the beginning of this section, we analyze how interband pairing is affected by $\hat{\mathcal{C}}_T$ symmetry. Finite energy pairing happens at interband momenta $\mathbf{k}_3$ where double-degenerate $|m_j| = 3/2$ electron states cross with $|m_j| = 1/2$ hole bands away from the Fermi energy. We can expand the interband pairing matrix $\hat{\Delta}_{\rm eff}^{+-}(\mathbf{k}_3)$ as

$$\hat{\Delta}_{\rm eff}^{+-}(\mathbf{k}_3) = \mathfrak{g}_{\mathbf{k}_3}^{+-}\cdot\hat{\tau}, \tag{54}$$

where $\mathfrak{g}_{\mathbf{k}_3}^{+-}$ is a four component vector given by

$$\mathfrak{g}_{\mathbf{k}_3}^{+-} = (\mathfrak{g}_{0,\mathbf{k}_3}^{+-}, \mathfrak{g}_{x,\mathbf{k}_3}^{+-}, \mathfrak{g}_{y,\mathbf{k}_3}^{+-}, \mathfrak{g}_{z,\mathbf{k}_3}^{+-}), \tag{55}$$

and $\hat{\tau} = (\hat{\tau}_0, \hat{\tau}_x, \hat{\tau}_y, \hat{\tau}_z)$ being the four component vector of Pauli matrices represented in interband pseudospin basis. Applying $\hat{\mathcal{C}}_T$ symmetry on $\hat{\tau}$ produce the same results as mentioned in Eq. (52) for $\hat{\sigma}$. In this case, $\hat{\tau}_0$ and $\hat{\tau}_z$ remain invariant along the $\langle 001 \rangle$ direction. Consequently, the interband pairing matrix becomes

$$\hat{\Delta}^{+-}_{\text{eff}}(k_z) = \mathfrak{g}^{+-}_{0,k_z}\hat{\tau}_0 + \mathfrak{g}^{+-}_{z,k_z}\hat{\tau}_z. \tag{56}$$

It is worth mentioning that $\hat{\tau}_0$ is allowed by the Pauli exclusion principle if we exchange band indices in addition to spin indices. Importantly, $\hat{\Delta}^{+-}_{\text{eff}}(k_z)$ is constrained by $\hat{\mathcal{C}}_T$ such that only up to two components of the $\mathfrak{g}^{+-}_{\mathbf{k}_2}$ vector are finite. This is identical with our analysis based on rotational symmetry in pseudospin basis described in Sec. II. The $\hat{\tau}_z$ remains invariant under two-fold rotation in pseudospin space combined with time-reversal symmetry.

Despite our pairing model is odd in parity, we can define an inversion operator in BdG form as

$$\hat{\mathcal{G}} = \text{diag}(\hat{I}_4, -\hat{I}_4) = \hat{\sigma}_z \otimes \hat{I}_4 \tag{57}$$

where

$$\hat{\mathcal{G}}\hat{H}_{\text{BdG}}(-\mathbf{k})\hat{\mathcal{G}}^{-1} = \hat{H}_{\text{BdG}}(\mathbf{k}). \tag{58}$$

In this case, the results given in Eqs. (53) and (56) hold true for $\hat{\mathcal{C}}_P$.

Importantly, such symmetries enforce the BdG Hamiltonian to become block diagonal along the topological phase transition directions and at finite excitation energies. This is a direct consequence of Eqs. (53) and (56). Although $\hat{\mathcal{C}}_T$ is anti-unitary, the twofold degeneracy can be lifted in the eigenspace of mirror reflection symmetry as

$$\hat{Y}^{-1}\hat{H}_{\text{BdG}}(k_z)\hat{Y} = \text{diag}\left(\hat{H}_{+i}(k_z), \hat{H}_{-i}(k_z)\right), \tag{59}$$

where $\hat{Y}$ is the matrix of eigenvectors for $\hat{\mathcal{C}}_P$ operator, and $\hat{H}_\lambda(\mathbf{k})$ is a 4×4 block labeled with eigenvalues of $\hat{P}\hat{C}_{2,x+y}$ as $\lambda = \pm i$. Note that $\hat{H}_{+i}(k_z) = \hat{H}_{-i}(k_z)$ with

$$\hat{H}_{+i}(k_z) = \begin{pmatrix} -E^+_{k_z} & 0 & 0 & \Delta k_z \\ 0 & -E^-_{k_z} & \Delta k_z & 0 \\ 0 & \Delta k_z & E^+_{k_z} & 0 \\ \Delta k_z & 0 & 0 & E^-_{k_z} \end{pmatrix}, \tag{60}$$

where $\Delta = (\sqrt{3}/2)\Delta$. The pairing sector is situated on the off-diagonal block of $\hat{H}_{\pm i}(\mathbf{k})$ with vanishing intraband pairing. $\hat{H}_{\pm i}(\mathbf{k})$ can be further brought into block diagonal form through the transformation $\hat{W}$ onto the interband basis. Such a transformation is given by

$$\begin{aligned}\hat{\mathscr{H}}'(k_z) &= \hat{W}^{-1}\left(\hat{Y}^{-1}\hat{H}_{\text{BdG}}(k_z)\hat{Y}\right)\hat{W} \\ &= \text{diag}\left(\hat{h}^{-+}_{k_z,+i}, \hat{h}^{+-}_{k_z,+i}, \hat{h}^{-+}_{k_z,-i}, \hat{h}^{+-}_{k_z,-i}\right),\end{aligned} \tag{61}$$

where

$$\hat{h}^{\nu\nu'}_{k_z,\lambda} = \begin{pmatrix} -E^{\nu'}_{k_z} & \Delta k_z \\ \Delta k_z & E^{\nu}_{k_z} \end{pmatrix}, \tag{62}$$

and

$$\hat{W} = \begin{pmatrix} 1&0&0&0&0&0&0&0 \\ 0&0&1&0&0&0&0&0 \\ 0&0&0&1&0&0&0&0 \\ 0&1&0&0&0&0&0&0 \\ 0&0&0&0&1&0&0&0 \\ 0&0&0&0&0&0&1&0 \\ 0&0&0&0&0&0&0&1 \\ 0&0&0&0&0&1&0&0 \end{pmatrix}. \tag{63}$$

Notably, Eq. (61) is identical to Eq. (6) of the main text. The effective Hamiltonian $\hat{\mathrm{H}}(k_x, k_y)$ for the helical surface states at finite excitation energies (see Eq. (8) of the main text) fulfills the symmetry relation

$$\hat{\mathcal{C}}_T\hat{\mathrm{H}}(k_x,k_y)\hat{\mathcal{C}}_T^{-1} = \hat{\mathcal{C}}_P\hat{\mathrm{H}}(k_x,k_y)\hat{\mathcal{C}}_P^{-1} = \hat{\mathrm{H}}(-k_y,-k_x). \tag{64}$$

V. STABILITY OF HELICAL DIRAC SURFACE STATES AT FINITE ENERGIES

To investigate the stability of helical topological surface states at finite excitation energies, we add randomness to chemical potential and magnetization of each layer in z-direction by

$$H_R(\mathbf{k}_{\shortparallel}, z) = \sum_{n_z}\sum_{\mathbf{k}_{\shortparallel}} \hat{\psi}^\dagger_{\mathbf{k}_{\shortparallel},z}\left(\mu_{n_z} + \mathbf{M}_{n_z}\cdot\hat{\mathbf{J}}\right)\hat{\psi}_{\mathbf{k}_{\shortparallel},z}, \tag{65}$$

where the basis in $j = 3/2$ representation is

$$\hat{\psi}^\dagger_{\mathbf{k}_{\shortparallel},z} = (c^\dagger_{\frac{3}{2},\mathbf{k}_{\shortparallel},z}, c^\dagger_{\frac{1}{2},\mathbf{k}_{\shortparallel},z}, c^\dagger_{-\frac{1}{2},\mathbf{k}_{\shortparallel},z}, c^\dagger_{-\frac{3}{2},\mathbf{k}_{\shortparallel},z}). \tag{66}$$

In Eq. (65), we consider k_z to be no longer conserved. Instead, $n_z = 0, ..., N_z$ is the layer index with N_z the total number of layers along the z-axis; $\sum_{\mathbf{k}_{\shortparallel}} = \sum_{k_x}\sum_{k_y}$, $\mathbf{k}_{\shortparallel} = (k_x, k_y)$ represents the conserved momenta; $\hat{\mathbf{J}} = (\hat{J}_x, \hat{J}_y, \hat{J}_z)$ is the vector of angular momenta; μ_{n_i} denotes the nonmagnetic onsite potential at layer n_i where the strength is a uniformly distributed random number within the interval $\mu_{n_i} \in [0, \Delta]$; the Zeeman field vector is $\mathbf{M}_{n_i} = (M_{x,n_i}, M_{y,n_i}, 0)$, with the strength $M_{x(y),n_i}$, taken as uniformly distributed random number in the interval $M_{x(y),n_i} \in [0, 0.06\Delta]$. The numerical results are shown in Fig. 4(a1-a3) and 4(b1-b3). We can observe in Fig. 4(a1) and (a2) that bulk and surface states become broadened while the topological surface states remain intact in the presence of nonmagnetic randomness at finite excitation energies since $\hat{C}_T$ symmetry is preserved. When the system is subjected to magnetic randomness,

the degeneracy of surface states are lifted due to broken time-reversal symmetry. In this case, $\hat{C}_T$ is broken. Along k_y direction (see Fig. 4(b2) and 4(b3)), the Dirac cone is gapped.

Furthermore, the symmetry $\hat{P}$ can be broken by introducing $\hat{H}_\delta(\mathbf{k})$ to Eq. (42), where $H_\delta(\mathbf{k})$ is defined as

$$\hat{H}_\delta(\mathbf{k}) = \delta \sum_i k_i \left(\hat{J}_{i+1}\hat{J}_i\hat{J}_{i+1} - \hat{J}_{i+2}\hat{J}_i\hat{J}_{i+2} \right), \qquad (67)$$

with δ denoting the strength of anti-symmetric spin-orbit coupling (ASOC). This term originates from T_d point group symmetry. Note that both $\hat{C}_{2,x+y}$ and $\hat{P}$ symmetries are absent in $\hat{H}_\delta(\mathbf{k})$ since

$$\hat{C}_{2,x+y}\hat{H}_\delta(\mathbf{k})\hat{C}^\dagger_{2,x+y} \neq \hat{H}_\delta(k_y, k_x, -k_z), \qquad (68)$$

$$\hat{P}\hat{H}_\delta(\mathbf{k})\hat{P}^\dagger \neq \hat{H}_\delta(\mathbf{k}). \qquad (69)$$

Consequently, $\hat{C}_T$ is broken due to absence of $\hat{C}_{2,x+y}$ symmetry. In this case, the low-energy superconducting nodes are lifted along the TPT directions for a sufficiently large δ (of the same order of symmetric spin-orbit coupling), and the topological surface states become unstable. To illustrate this, the excitation spectra are plotted in Figs. 4 (c1-c3) in the presence of $H_\delta(\mathbf{k})$. Clearly, the surface states emerging from the finite energy gap closing point hybridize with the bulk states at large momentum. This can be understood from Eq. (6) since then the block digonalization is no applicable.

This analysis identifies $\hat{C}_T$ symmetry is required for the stability of the surface states.

VI. HELICAL DIRAC SURFACE STATES AT FINITE ENERGIES

In this section, we provide details for the derivation of the helical Dirac surface states described in the main text. The BdG Hamiltonian along the [001] direction becomes

$$\hat{H}(k_z) = \begin{pmatrix} \hat{H}_1 & 0 & \hat{H}_3 & 0 \\ 0 & \hat{H}_2 & 0 & \hat{H}_3 \\ \hat{H}_3 & 0 & -\hat{H}_1 & 0 \\ 0 & \hat{H}_3 & 0 & -\hat{H}_2 \end{pmatrix}, \qquad (70)$$

with

$$\hat{H}_1 = \mathrm{diag}(E^+_{k_z}, E^-_{k_z}),\ \hat{H}_2 = \mathrm{diag}(E^-_{k_z}, E^+_{k_z}), \qquad (71)$$

where $E^+_{k_z} = (\alpha + 9\beta/4)k_z^2 - \mu$, $E^-_{k_z} = (\alpha + \beta/4)k_z^2 - \mu$, $\hat{H}_3 = \mathbf{\Delta} k_z \hat{\sigma}_x$, and $\mathbf{\Delta} = \sqrt{3}\Delta/2$. To be able to apply our theory, presented in Eqs. (2-6) of the main text, we should represent $\hat{H}(k_z)$ in the pseudospin basis where each diagonal block contains a pair of doubly degenerate

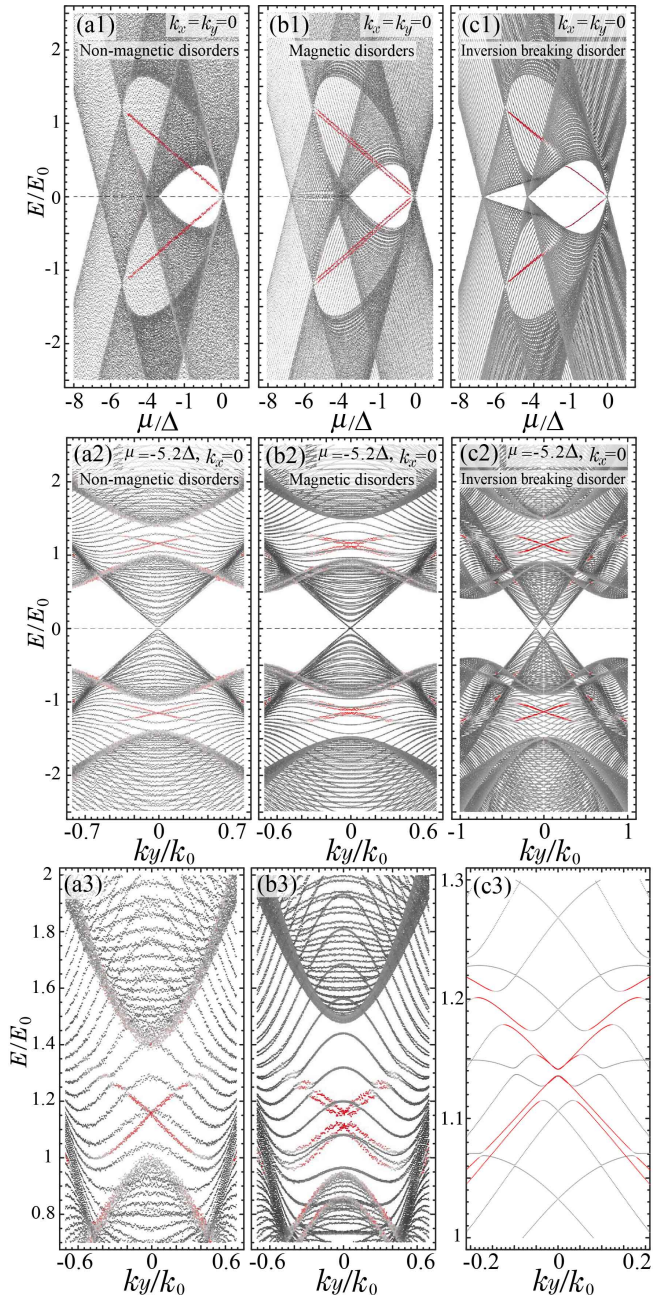

Figure 4. Excitation spectrum for (001) slab in the presence of nonmagnetic randomness with strength (a1) $v_i \in \{0, \Delta\}$ for 120 layers, (a2,a3) $v_i \in \{0, 0.6\Delta\}$ for 80 layers, (b2-b3) magnetic randomness with the form $M_{x,n_i}\hat{J}_x + M_{y,n_i}\hat{J}_y$ with $M_{x(y),n_i} \in \{0, 0.2\Delta\}$ for 80 layers (c1-c3) inversion symmetry breaking spin-orbit coupling $\delta = 0.3\Delta$ for 120 layers. Panels (a3), (b3) and (c3) are the enlarged view of the top panels. Other parameters are $(\alpha, \beta, \gamma, \mu) = -(1, 0.3, 1, 5.2)\Delta$. Note that $\gamma \neq \beta$ indicates broken O(3) symmetry in the normal state. The extended bulk (surface) states are illustrated by gray (red) color according to inverse participation ratio.

bands. This can be done through the unitary transformation $\hat{\mathscr{U}}_1$

$$\hat{H}_1(k_z) = \hat{\mathscr{U}}_1^\dagger H(k_z)\hat{\mathscr{U}}_1 \tag{72}$$

$$= \begin{pmatrix} E^+_{k_z} & 0 & 0 & \boldsymbol{\Delta} k_z \\ 0 & E^-_{k_z} & \boldsymbol{\Delta} k_z & 0 \\ 0 & \boldsymbol{\Delta} k_z & -E^+_{k_z} & 0 \\ \boldsymbol{\Delta} k_z & 0 & 0 & -E^-_{k_z} \end{pmatrix} \otimes \hat{\sigma}_0, \tag{73}$$

where the unitary matrix $\hat{\mathscr{U}}_1^\dagger = \hat{\mathscr{U}}_1^{-1}$ is given by

$$\hat{\mathscr{U}}_1 = \begin{pmatrix} 1&0&0&0&0&0&0&0 \\ 0&0&1&0&0&0&0&0 \\ 0&0&0&1&0&0&0&0 \\ 0&1&0&0&0&0&0&0 \\ 0&0&0&0&1&0&0&0 \\ 0&0&0&0&0&0&1&0 \\ 0&0&0&0&0&0&0&1 \\ 0&0&0&0&0&1&0&0 \end{pmatrix}. \tag{74}$$

In the next step, Eq. (73) should be represented in the interband basis. This can be done through another unitary transformation $\hat{\mathscr{U}}_2$ as

$$\hat{\mathscr{H}}(k_z) = \hat{\mathscr{U}}_2^\dagger \hat{H}_1(k_z)\hat{\mathscr{U}}_2 = (\hat{\mathscr{U}}_1\hat{\mathscr{U}}_2)^\dagger H(k_z)\hat{\mathscr{U}}_1\hat{\mathscr{U}}_2 \tag{75}$$

$$= \begin{pmatrix} \hat{\mathsf{H}}^{+-}_{k_z} & 0 \\ 0 & \hat{\mathsf{H}}^{-+}_{k_z} \end{pmatrix}, \tag{76}$$

where

$$\hat{\mathsf{H}}^{+-}_{k_z} = \begin{pmatrix} E^+_{k_z} & \boldsymbol{\Delta} k_z \\ \boldsymbol{\Delta} k_z & -E^-_{k_z} \end{pmatrix} \otimes \hat{\sigma}_0, \tag{77}$$

$$\hat{\mathsf{H}}^{-+}_{k_z} = \begin{pmatrix} E^-_{k_z} & \boldsymbol{\Delta} k_z \\ \boldsymbol{\Delta} k_z & -E^+_{k_z} \end{pmatrix} \otimes \hat{\sigma}_0. \tag{78}$$

The transformation $\hat{\mathscr{U}}_2$ fulfills the unitary property $\hat{\mathscr{U}}_2^\dagger = \hat{\mathscr{U}}_2^{-1}$. Its explicit matrix form is given by

$$\hat{\mathscr{U}}_2 = \begin{pmatrix} 0&1&0&0&0&0&0&0 \\ 1&0&0&0&0&0&0&0 \\ 0&0&0&0&0&1&0&0 \\ 0&0&0&0&1&0&0&0 \\ 0&0&0&0&0&0&0&1 \\ 0&0&0&0&0&0&1&0 \\ 0&0&0&1&0&0&0&0 \\ 0&0&1&0&0&0&0&0 \end{pmatrix}. \tag{79}$$

Note that $\hat{\mathscr{H}}(k_z)$, given in Eq. (76), is identical to Eq. (2) of the main text. In this case, $\boldsymbol{\Delta} k_z \hat{\sigma}_0$ is the FE pairing potential in Eqs. (77) and Eqs. (78). The zeros on the off-diagonal blocks of Eq. (76) indicate vanishing intraband pairing giving rise to the presence of nodes at the Fermi energy. The diagonal blocks in $\hat{\mathscr{H}}(k_z)$ exhibit pseudospin-π rotation symmetry along the z(x)-axis, i.e., the symmetry relations given in Eqs. (27) and (29). The explicit matrix form for such an operator can be obtained as

$$\hat{\mathcal{D}}_{\mathbf{n}_z}(\pi,-1) = \begin{pmatrix} 0&i&0&0 \\ i&0&0&0 \\ 0&0&0&i \\ 0&0&i&0 \end{pmatrix}.$$

Thus, Eq. (76) is further reducible in the eigenspace of $\hat{\mathcal{D}}_{\mathbf{n}_z}(\pi,-1)$. This can be done through the unitary matrix $\hat{\mathscr{U}}_3$

$$\hat{\mathscr{H}}'(k_z) = \hat{\mathscr{U}}_3^\dagger \hat{\mathscr{H}}(k_z)\hat{\mathscr{U}}_3 \tag{80}$$

$$= (\hat{\mathscr{U}}_1\hat{\mathscr{U}}_2\hat{\mathscr{U}}_3)^\dagger H(k_z)\hat{\mathscr{U}}_1\hat{\mathscr{U}}_2\hat{\mathscr{U}}_3 \tag{81}$$

$$= \mathrm{diag}(\hat{h}^{+-}_{k_z,+}, \hat{h}^{+-}_{k_z,+}, \hat{h}^{-+}_{k_z,+}, \hat{h}^{-+}_{k_z,-}), \tag{82}$$

with

$$\hat{h}^{+-}_{k_z,\pm} = \begin{pmatrix} -E^-_{k_z} & \boldsymbol{\Delta} k_z \\ \boldsymbol{\Delta} k_z & E^+_{k_z} \end{pmatrix}, \ \hat{h}^{-+}_{k_z,\pm} = \begin{pmatrix} -E^+_{k_z} & \boldsymbol{\Delta} k_z \\ \boldsymbol{\Delta} k_z & E^-_{k_z} \end{pmatrix}, \tag{83}$$

and $\hat{\mathscr{U}}_3 = \mathrm{diag}(\hat{\mathscr{V}}, \hat{\mathscr{V}})$ where $\hat{\mathscr{V}}$ is the matrix of eigenvectors of $\hat{\mathcal{D}}_{\mathbf{n}_z}(\pi,-1)$ given by

$$\hat{\mathscr{V}} = \frac{1}{\sqrt{2}} \begin{pmatrix} 0&1&0&-1 \\ 0&1&0&1 \\ 1&0&-1&0 \\ 1&0&1&0 \end{pmatrix}.$$

We solve the eigenvalue problem for one of the decoupled subblocks in Eq. (82). This problem is given by $\hat{h}^{-+}_{k_z,\pm}\hat{\Phi}(\xi,z) = \mathscr{E}_{\mathrm{DP}}\hat{\Phi}(\xi,z)$ where $\hat{\Phi}(\xi,z) = (u,v)^T \exp(\xi z)$ is the ansatz for the decaying eigenspinor. ξ denotes the localization factor, $|u|^2$ ($|v|^2$) is the probability weight for electron (hole) states with different magnetic quantum number $m_j = \pm 3/2$ ($m_j = \pm 1/2$). We consider a semi-infinite system in $z \geq 0$ space. Therefore, k_z is no longer conserved and we use its real space representation $k_z = k_z^\dagger = -i\partial_z$. In this case, the secular equation $(\hat{h}^{-+}_{-i\partial_z,\pm} - \mathscr{E}_{\mathrm{DP}})\hat{\Phi}(\xi,z) = 0$ can be evaluated by setting its determinant to zero,

$$\begin{vmatrix} m'\xi^2 + \mu - \mathscr{E}_{\mathrm{DP}} & -i\boldsymbol{\Delta}\xi \\ -i\boldsymbol{\Delta}\xi & -(m\xi^2+\mu) - \mathscr{E}_{\mathrm{DP}} \end{vmatrix} = 0, \tag{84}$$

where $m = \alpha + \beta/4$ and $m' = \alpha + 9\beta/4$. The solution of the secular equation yields

$$\xi_\pm = \sqrt{\frac{1}{2mm'}\left(\Lambda \pm \sqrt{\Lambda^2 + 4mm'(\mathscr{E}_{\mathrm{DP}}^2 - \mu^2)}\right)}, \tag{85}$$

where $\Lambda = \boldsymbol{\Delta}^2 - \mathscr{E}_{\mathrm{DP}}\vartheta^- - \mu\vartheta^+$ and $\vartheta^\pm = (m' \pm m)/2$. In the absence of pairing, i.e., for $\boldsymbol{\Delta} = 0$, the localization length becomes purely imaginary leading to extended states. However, $\xi_\pm$ obtains a real component in

the topological phase induced by FE pairing. This leads to proper surface state solutions.

To specify the components of $\hat{\Phi}(\xi,z)$, we use the secular equation, and obtain

$$u\equiv u_\iota=-i\mathbf{\Delta}\xi_\iota\rightarrow v\equiv v_\iota=m'\xi_\iota^2+\mu-\mathscr{E}_{\rm DP}, \quad (86)$$

$$v\equiv V_\iota=-i\mathbf{\Delta}\xi_\iota\rightarrow u\equiv U_\iota=m\xi_\iota^2+\mu+\mathscr{E}_{\rm DP}. \quad (87)$$

Consequently, we have a pair of eigenspinors given by

$$\hat{\Phi}(\xi_\iota,z)=\begin{pmatrix}u_\iota\\ v_\iota\end{pmatrix}e^{\xi_\iota z},\quad \hat{\Phi}'(\xi_\iota,z)=\begin{pmatrix}U_\iota\\ V_\iota\end{pmatrix}e^{\xi_\iota z}. \quad (88)$$

We can construct two sets of wave functions by the superposition of eigenspinors $\hat{\Phi}(\xi_\iota,z)$ $(\hat{\Phi}'(\xi,z))$,

$$\hat{\Psi}_1(z)=\sum_{\iota=\pm}C_\iota\hat{\Phi}(\xi_\iota,z),\quad \hat{\Psi}_2(z)=\sum_{\iota=\pm}Q_\iota\hat{\Phi}'(\xi_\iota,z), \quad (89)$$

where the summations run over the decay factors and the coefficients of the expansion are denoted by C_ι and Q_ι. To have surface state solutions, the wave functions and their first derivatives must vanish at the interface of the system and far away from the interface, i.e.,

$$\hat{\Psi}(\infty)=\hat{\Psi}'(\infty)=0,\quad \hat{\Psi}(0)=\hat{\Psi}'(0)=0. \quad (90)$$

Note that we assume just one interface in our analytical calculations. The boundary conditions at $z=0$ give rise to two pairs of equations

$$C_-\begin{pmatrix}u_-\\ v_-\end{pmatrix}+C_+\begin{pmatrix}u_+\\ v_+\end{pmatrix}=0, \quad (91)$$

$$Q_-\begin{pmatrix}U_-\\ V_-\end{pmatrix}+Q_+\begin{pmatrix}U_+\\ V_+\end{pmatrix}=0. \quad (92)$$

Re-arranging Eqs. (91) and (92), we arrive at

$$\frac{C_-}{C_+}=-\frac{\xi_+}{\xi_-}=-\frac{m'\xi_+^2+\mu-\mathscr{E}_{\rm DP}}{m'\xi_-^2+\mu-\mathscr{E}_{\rm DP}}, \quad (93)$$

$$\frac{Q_-}{Q_+}=-\frac{\xi_+}{\xi_-}=-\frac{m\xi_+^2+\mu+\mathscr{E}_{\rm DP}}{m\xi_-^2+\mu+\mathscr{E}_{\rm DP}}. \quad (94)$$

Combining Eqs. (93) and (94) results in the explicit formula for the energy of the helical Dirac surface points $\mathscr{E}_{\rm DP}$ given in Eq. (7) of the main text.

Choosing $C_-=Q_-=\xi_+$ and $C_+=Q_+=-\xi_-$, this allows us to derive the general eigenfunction corresponding to $\mathscr{E}_{\rm DP}$,

$$\hat{\Psi}(z)=\mathcal{C}\xi_+\begin{pmatrix}i\mathbf{\Delta}\xi_-\\ m'\xi_-^2+\mu-\mathscr{E}_{\rm DP}\end{pmatrix}(e^{-\xi_-z}-e^{-\xi_+z}), \quad (95)$$

where $\mathcal{C}$ is the normalization factor

$$\mathcal{C}=\frac{1}{\sqrt{(|\kappa_1|^2+|\kappa_2|^2)}}\frac{1}{\sqrt{\int_0^\infty dz\ |f(z)|^2}}. \quad (96)$$

VII. EFFECTIVE 2D HELICAL SURFACE HAMILTONIAN

In this section, we derive the effective Hamiltonian for the 2D helical surface states given in Eq. (8) of the main text. To do so, we need to project the bare BdG Hamiltonian onto the helical Dirac surface states basis. Note that $\hat{\Psi}(z)$ in Eq. (95) is the eigenfunction corresponding to the subblock matrix $\hat{h}^{-+}_{\mathbf{k},+}$, and we have defined $f(z)\equiv(e^{-\xi_-z}-e^{-\xi_+z})$, $\kappa_1\equiv i\mathbf{\Delta}\xi_+\xi_-$, and $\kappa_2\equiv\xi_+(m'\xi_-^2+\mu-\mathscr{E}_{\rm DP})$. To have a proper projection basis, we also need the eigenfunction for the subblock $\hat{h}^{+-}_{\mathbf{k},+}$. It is given by $\hat{\varphi}(z)=\mathcal{C}(\kappa_3,\kappa_4)^T\gamma(z)$ where $\kappa_3\equiv\xi_+(m\xi_-^2+\mu+\mathscr{E}_{\rm DP})$, $\kappa_4\equiv-i\Delta\xi_+\xi_-$, and $\gamma(z)=-f(z)$.

$\hat{\Psi}(z)$ and $\hat{\varphi}(z)$ are 2×1 column vectors. In order to use them for the projection method, we convert them to 8×1 representation since the BdG Hamiltonian is a 8×8 matrix. This can be done through the transformation made by the 8×2 columns of the matrix $\hat{\mathscr{U}}^{-1}=\{\hat{\gamma}_1,\hat{\gamma}_2,\hat{\gamma}_3,\hat{\gamma}_4\}$. The first and forth subblock matrices in Eq. (82) are identical corresponding to $\hat{h}^{-+}_{\mathbf{k},+}$ and $\hat{h}^{-+}_{\mathbf{k},-}$, respectively. Thus, they correspond to doubly degenerate helical surface states with eigenvalue $\mathscr{E}_{\rm DP}$. Therefore, their 8×1 representations take the form

$$\hat{\Gamma}_1^-\equiv\hat{\gamma}_1\hat{\Psi}(z)=\mathcal{C}f(z)(0,\kappa_2,0,0,\kappa_1,0,0,0)^T, \quad (97)$$

$$\hat{\Gamma}_2^-\equiv\hat{\gamma}_4\hat{\Psi}(z)=\mathcal{C}f(z)(0,0,\kappa_2,0,0,0,0,\kappa_1)^T. \quad (98)$$

We repeat the above steps for $\hat{\varphi}(z)$ to obtain the proper basis for the sectors $\hat{h}^{+-}_{\mathbf{k},+}$ and $\hat{h}^{+-}_{\mathbf{k},-}$,

$$\hat{\Gamma}_1^+\equiv\hat{\gamma}_2\hat{\varphi}(z)=\mathcal{C}\gamma(z)(\kappa_4,0,0,0,0,\kappa_3,0,0)^T, \quad (99)$$

$$\hat{\Gamma}_2^+\equiv\hat{\gamma}_3\hat{\varphi}(z)=\mathcal{C}\gamma(z)(0,0,0,\kappa_4,0,0,\kappa_3,0)^T. \quad (100)$$

We use Eqs. (97-100) as the proper orthonormal set of eigenfunctions to project the bulk superconducting Hamiltonian to the surface. Note that the orthonormality condition reads $\int_0^\infty dz[\hat{\mathscr{Y}}^\nu]^\dagger\hat{\mathscr{Y}}^\nu=\hat{\sigma}_0$ where $\hat{\mathscr{Y}}^\pm=\{\hat{\Gamma}_1^\pm,\hat{\Gamma}_2^\pm\}$.

To derive the effective Hamiltonian for the 2D helical surface states, we consider the conserved wave vectors k_x and k_y in the BdG Hamiltonian to be small close to the Γ point. Then, we project $\hat{H}(k_x,k_y,-i\partial_z)$ onto the basis of the helical Dirac surface states. Thus, the effective Hamiltonian at finite excitation energies becomes

$$\hat{\mathtt{H}}(k_x,k_y)=\int_0^\infty dz\hat{\mathscr{Y}}^{\nu\dagger}(z)\hat{H}(k_x,k_y,-i\partial_z)\hat{\mathscr{Y}}^\nu(z)=\begin{pmatrix}A_{1,1}&A_{1,2}\\ A_{2,1}&A_{2,2}\end{pmatrix}, \quad (101)$$

where the matrix elements of $\hat{\mathtt{H}}(k_x,k_y)$ are given by

$$A_{i,j}=\int_0^\infty dz\hat{\Gamma}_i^\dagger(z)\hat{H}(k_x,k_y,-i\partial_z)\hat{\Gamma}_j(z), \quad (102)$$

J	O_h	η	$\hat{\mathcal{O}}_\eta(\hat{J})$	$\hat{\eta}$	(L,S)	(L,S)
0	$A_{1g,u}$	$A_{1g,u}$	$\frac{1}{2}\hat{I}_4$	$\hat{A}_{1g,u}=\hat{\mathcal{N}}_{0,0}$	$(0,0)$	$(1,1)$
1	T_{1u}	$T^{(1)}_{1u}$	$\frac{1}{\sqrt{5}}\hat{J}_z$	$\hat{T}^{(1)}_{1u}=\hat{\mathcal{N}}_{1,0}$	$\times$	$(1,1)$
		$T^{(2)}_{1u}$	$\frac{1}{\sqrt{5}}\hat{J}_y$	$\hat{T}^{(2)}_{1u}=\frac{i}{\sqrt{2}}(\hat{\mathcal{N}}_{1,-1}+\hat{\mathcal{N}}_{1,1})$	$\times$	$(1,1)$
		$T^{(3)}_{1u}$	$\frac{1}{\sqrt{5}}\hat{J}_x$	$\hat{T}^{(3)}_{1u}=\frac{1}{\sqrt{2}}(\hat{\mathcal{N}}_{1,-1}-\hat{\mathcal{N}}_{1,1})$	$\times$	$(1,1)$
2	$E_{g,u}$	$E^{(1)}_{g,u}$	$\frac{1}{6}(3\hat{J}_z^2-\hat{\mathbf{J}})$	$\hat{E}^{(1)}_{g,u}=\hat{\mathcal{N}}_{2,0}$	$(0,2)$	$(1,1),(1,3)$
		$E^{(2)}_{g,u}$	$\frac{1}{2\sqrt{3}}(\hat{J}_x^2-\hat{J}_y^2)$	$\hat{E}^{(2)}_{g,u}=\frac{1}{\sqrt{2}}(\hat{\mathcal{N}}_{2,-2}+\hat{\mathcal{N}}_{2,2})$	$(0,2)$	$(1,1),(1,3)^*$
	$T_{2g,u}$	$T^{(1)}_{2g,u}$	$\frac{1}{\sqrt{3}}(\hat{J}_x\hat{J}_y+\hat{J}_y\hat{J}_x)$	$\hat{T}^{(1)}_{2g,u}=\frac{i}{\sqrt{2}}(\hat{\mathcal{N}}_{2,-2}-\hat{\mathcal{N}}_{2,2})$	$(0,2)$	$(1,1),(1,3)^*$
		$T^{(2)}_{2g,u}$	$\frac{1}{\sqrt{3}}(\hat{J}_z\hat{J}_x+\hat{J}_x\hat{J}_z)$	$\hat{T}^{(2)}_{2g,u}=\frac{i}{\sqrt{2}}(\hat{\mathcal{N}}_{2,-1}-\hat{\mathcal{N}}_{2,1})$	$(0,2)$	$(1,1),(1,3)^*$
		$T^{(3)}_{2g,u}$	$\frac{1}{\sqrt{3}}(\hat{J}_y\hat{J}_z+\hat{J}_z\hat{J}_y)$	$\hat{T}^{(3)}_{2g,u}=\frac{i}{\sqrt{2}}(\hat{\mathcal{N}}_{2,-1}+\hat{\mathcal{N}}_{2,1})$	$(0,2)$	$(1,1),(1,3)^*$
3	A_{2u}	A_{2u}	$\frac{1}{\sqrt{3}}(\hat{J}_x\hat{J}_y\hat{J}_z+\hat{J}_z\hat{J}_y\hat{J}_x)$	$\hat{A}_{2u}=\frac{i}{\sqrt{2}}(\hat{\mathcal{N}}_{2,-2}-\hat{\mathcal{N}}_{2,2})$	$\times$	$(1,3)^*$
	T_{1u}	$T^{(1)}_{1u}$	$\frac{4}{\sqrt{365}}\hat{J}_z^3$	$\hat{T}^{(1)}_{1u}=\frac{12}{5\sqrt{73}}\hat{\mathcal{N}}_{3,0}$	$\times$	$(1,3)$
		$T^{(2)}_{1u}$	$\frac{4}{\sqrt{365}}\hat{J}_y^3$	$\hat{T}^{(2)}_{1u}=\frac{3}{5\sqrt{73}i}[\sqrt{5}(\hat{\mathcal{N}}_{3,-3}+\hat{\mathcal{N}}_{3,3})+\sqrt{3}(\hat{\mathcal{N}}_{3,1}+\hat{\mathcal{N}}_{3,-1})]$	$\times$	$(1,3)$
		$T^{(3)}_{1u}$	$\frac{4}{\sqrt{365}}\hat{J}_x^3$	$\hat{T}^{(3)}_{1u}=\frac{3}{5\sqrt{73}}[\sqrt{5}(\hat{\mathcal{N}}_{3,-3}-\hat{\mathcal{N}}_{3,3})+\sqrt{3}(\hat{\mathcal{N}}_{3,1}-\hat{\mathcal{N}}_{3,-1})]$	$\times$	$(1,3)$
	T_{2u}	$T^{(1)}_{2u}$	$\frac{1}{\sqrt{3}}\lceil\hat{J}_z(\hat{J}_x^2-\hat{J}_y^2)\rfloor$	$\hat{T}^{(1)}_{2u}=\frac{1}{\sqrt{2}}(\hat{\mathcal{N}}_{3,-2}+\hat{\mathcal{N}}_{3,2})$	$\times$	$(1,3)^*$
		$T^{(2)}_{2u}$	$\frac{1}{\sqrt{3}}\lceil\hat{J}_x(\hat{J}_y^2-\hat{J}_z^2)\rfloor$	$\hat{T}^{(2)}_{2u}=\frac{1}{4}[\sqrt{3}(\hat{\mathcal{N}}_{3,3}-\hat{\mathcal{N}}_{3,-3})+\sqrt{5}(\hat{\mathcal{N}}_{3,1}-\hat{\mathcal{N}}_{3,-1})]$	$\times$	$(1,3)^*$
		$T^{(3)}_{2u}$	$\frac{1}{\sqrt{3}}\lceil\hat{J}_y(\hat{J}_z^2-\hat{J}_x^2)\rfloor$	$\hat{T}^{(3)}_{2u}=\frac{1}{4i}[\sqrt{3}(\hat{\mathcal{N}}_{3,3}+\hat{\mathcal{N}}_{3,-3})-\sqrt{5}(\hat{\mathcal{N}}_{3,1}+\hat{\mathcal{N}}_{3,-1})]$	$\times$	$(1,3)^*$

Table II. Decomposition of total angular momentum J (first column) in the irreducible representation (irrep) of O_h symmetry (second column). The dimension of an irrep is distinguished by the number of components η given in the third column. The fourth column denotes the normalized irreducible basis matrices for a component of O_h symmetry in $j=3/2$ representation. The fifth column demonstrates the correspondence between the matrix form for components of a cubic irrep $\hat{\eta}$ and the components of $SO(3)$ symmetry, namely $\hat{\mathcal{N}}_{J,m_j}$ being the total angular momentum tensor matrices. The last two columns indicate the spin S and orbital L angular momenta of Cooper pairs associated to J and components of a given irrep. The Fermi statistics forces both L and S to be even (g) or odd (u). The symmetrization of the basis matrices is denoted by $\lceil\hat{A}\hat{B}\hat{C}\rfloor=(\hat{A}\hat{B}\hat{C}+\hat{A}\hat{C}\hat{B}+\hat{B}\hat{C}\hat{A}+\hat{B}\hat{A}\hat{C}+\hat{C}\hat{A}\hat{B}+\hat{C}\hat{B}\hat{A})/3!$. The pairing channels satisfying TPT at FEs are marked by $(*)$.

with $i,j\in\{1,2\}$. $\hat{\mathtt{H}}(k_x,k_y)$ should be Hermitian, thus, the matrix elements in Eq. (101) must fulfill the relations

$$A_{1,1}=A^*_{1,1}=A_{2,2}=A^*_{2,2}, \tag{103}$$

$$A_{1,2}=A^*_{2,1},\quad A_{2,1}=A^*_{1,2}. \tag{104}$$

After straightforward algebra, we arrive at the 2D effective Hamiltonian for the helical surface states given in Eq. (8) of the main text. Note that the group velocity of the helical topological Dirac surface states at finite excitation energies takes the form

$$\varsigma_2=\frac{\sqrt{3}}{4}\frac{\Delta}{(|\kappa_1|^2+|\kappa_2|^2)}\mathrm{Im}\left[(\kappa_2\kappa_1^*-\kappa_1\kappa_2^*)\right]. \tag{105}$$

It is clear that ς_2 depends on the components of the wave function with direct proportionality to the pairing strength Δ.

VIII. ENERGY SCALE FOR FINITE-ENERGY COOPER PAIRING IN WEAKLY HOLE-DOPED YPdBi

In this section, we estimate the energy scale for finite-energy Cooper pairing in weakly hole-doped YPdBi. We obtain a range of $\Delta_E\approx 7.7-46.2$ μeV, which can be resolved in state-of-the-art scanning tunneling microscope (STM) [8]. We first refer to the normal state band structure of YPdBi calculated by density functional theory (DFT), see Fig. 5(a).

Close to the Γ point, the electronic structure hosts two branches of the Γ_8 bands curving downward in an energy window around ≈ 0.7eV before other bands coexists with the Γ_8 bands. This material is a non-centrosymmetric semimetal, which becomes superconductor at $T_c=1.6$ K [9]. The absence of inversion symmetry results in weak ASOC, which leads to a mixed-parity superconducting state. Specifically, when the chemical potential resides in the $j=3/2$ bands, the mixed-parity pairing state $A_{1g}+A_{2u}$ should be favorable in YPdBi due to T_d symmetry [10].

In the following, we estimate the value of finite-energy pairing in YPdBi. To this end, we employ a combination of DFT and analytical model analysis [11]. Our DFT calculations rely on the Kohn-Sham-Bogoliubov-de-Gennes (KS-BdG) method as implemented in the relativistic full-potential JuKKR code [12, 13]. The crystal structure for YPdBi is taken from the materials project [14, 15], where we use a compressed lattice constant by 3% to clearly isolate the Γ_8 bands from the Γ_6 and Γ_7 bands [16]. We employ the local density approximation for the normal-state exchange-correlation functional [17] and include the effects of spin-orbit coupling as well as an angular mo-

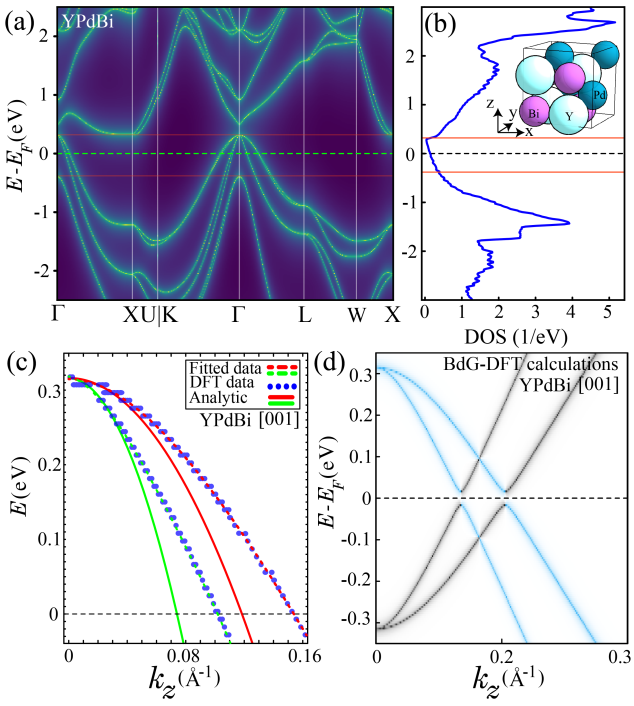

Figure 5. (a) DFT normal state band structure for YPdBi. (b) Density of states for the band structure shown in (a). (c) DFT band structure in [001] direction (marked by blue filled circles), fit to the DFT data (dashed lines) and $\mathbf{k}\cdot\mathbf{p}$ model (solid lines). (d) BdG-DFT band structure in [001] direction for $\Delta_s \neq 0$ and $\Delta_p = 0$. The blue (black) coloring of the bands denote their particle (hole) character.

mentum cutoff of $\ell_{\max} = 3$ in the expansion of the basis into spherical harmonics. The Fermi level is shifted down such that μ lies in the range where only the Γ_8 bands persist, as indicated in Fig. 5(a). Note that the low density of states in this energy range, see Fig. 5(b), allows to tune the chemical potential easily, which could be achievable experimentally via electron irradiation or by suitable electrical gating [10].

To illustrate the need for an unconventional A_{2u} pairing channel for the existence of finite energy pairing, we first consider only a constant s-wave pairing channel A_{1g} in our DFT-based KS-BdG simulations with a (for illustration purposes) large magnitude of $\Delta_s = 1$ mRy within the atoms of the YPdBi unit cell.

The normal state and superconducting band structure along the [001] direction are depicted in Figs. 5(c) and 5(d), respectively. In both panels, the system is weakly hole doped, such that the chemical potential lies in the $j = 3/2$ bands, close to the Γ point. Clearly, the $j = 3/2$ bands have an identical sign of the curvature at the Fermi energy, i.e., both curl downward. The energy bands are doubly degenerate, protected by a combination of time-reversal and mirror-reflection symmetry [18]. Using Eqs. (42) and (67), we obtain the $\mathbf{k}\cdot\mathbf{p}$ spectrum given by

$$E^{\pm}_{\mathbf{k}} = (\alpha + \frac{5}{4}\beta)k_z^2 \pm \beta\sqrt{k_z^4 + \frac{3}{4}\frac{\delta^2}{\beta^2}k_z^2} - \mu. \tag{106}$$

We fit the DFT data up to the second order polynomials. Then, comparing these with Eq. (106), we extract the model parameters for weakly hole-doped YPdBi close to the Γ point as

$$\begin{aligned} &\alpha = -18.1\,\text{Å}^2\text{eV}, && \beta = -17.5\,\text{Å}^2\text{eV}, \\ &\gamma = 16.1\,\text{Å}^2\text{eV} && \delta = -0.1\,\text{ÅeV}, \\ &\mu = -317\,\text{meV}. \end{aligned} \tag{107}$$

Note that the parameter describing ASOC δ is weak compared to the symmetric spin-orbit coupling β, i.e., $\delta/\beta \approx 0.00571\,\text{Å}^{-1}$.

We further analyze the effects of interband pairing in a (001) slab of YPdBi. The numerical calculations are done by tight-binding regularization of the $\mathbf{k}\cdot\mathbf{p}$ model given in Eqs. (42) and (67). The results are illustrated in Fig. 6, where we assume open (periodic) boundary conditions along z-direction (x- and y-directions). In Figs. 6(a1-a3) and 6(b1-b3), the spectra are shown for a pure odd-parity septet channel $\hat{\Delta}^{(A_{2u})}_{\mathbf{k}}$ and mixed-parity $\Delta_{\mathbf{k}} = \hat{\Delta}^{(A_{1g})}_{\mathbf{k}} + \hat{\Delta}^{(A_{2u})}_{\mathbf{k}}$ channel, respectively. The matrix form for the corresponding pairing state is explicitly given by

$$\hat{\Delta}^{(A_{1g})}_{\mathbf{k}} = \Delta_s \begin{pmatrix} 0 & 0 & 0 & 1 \\ 0 & 0 & -1 & 0 \\ 0 & 1 & 0 & 0 \\ -1 & 0 & 0 & 0 \end{pmatrix}, \tag{108}$$

$$\hat{\Delta}^{(A_{2u})}_{\mathbf{k}} = \Delta_p \begin{pmatrix} \frac{3}{4}k_- & \frac{\sqrt{3}}{2}k_z & \frac{\sqrt{3}}{4}k_+ & 0 \\ \frac{\sqrt{3}}{2}k_z & \frac{3}{4}k_+ & 0 & -\frac{\sqrt{3}}{4}k_- \\ \frac{\sqrt{3}}{4}k_+ & 0 & -\frac{3}{4}k_- & \frac{\sqrt{3}}{2}k_z \\ 0 & -\frac{\sqrt{3}}{4}k_- & \frac{\sqrt{3}}{2}k_z & -\frac{3}{4}k_+ \end{pmatrix}, \tag{109}$$

where $\Delta_{s(p)}$ denotes the strength for the s(p)-wave A_{1g} (A_{2u}) pairing channel. Both $\mathbf{k}\cdot\mathbf{p}$ and DFT calculations imply that interband pairing is absent in the A_{1g} pairing channel, i.e., $\hat{\Delta}^{+-}_{\mathbf{k}} = 0$. This is because the s-wave pairing is isotropic in momentum space. However, interband pairing is present in the A_{2u} channel. This is the reason for the reduced density of bulk states at finite excitation energies in the range $|E/E_0| \in [0.5, 1]$, marked by yellow lines in Figs. 6(a2) and 6(b2). Using the $\mathbf{k}\cdot\mathbf{p}$ theory, the size of the interband pairing for the pure A_{2u} channel (in the limit $\delta/\beta \to 0$) becomes [19]

$$\Delta_E = \sqrt{2}\sqrt{\text{Tr}(\hat{\Delta}^{+-}_{\tilde{k}_z}[\hat{\Delta}^{+-}_{\tilde{k}_z}]^{\dagger})}, \tag{110}$$

where $\hat{\Delta}^{+-}_{\tilde{k}_z}$ denotes the interband pairing matrix. The relevant electron-hole hybridization takes place at momenta $\tilde{k}_z = \pm 2[\mu/(4\alpha + 5\beta)]^{1/2}$ and at finite excitation

energies. Along the [001] direction (and equivalent directions), we obtain $\mathrm{Tr}(\hat{\Delta}^{+-}_{\tilde{k}_z}[\hat{\Delta}^{+-}_{\tilde{k}_z}]^\dagger) = 3\Delta_p^2\tilde{k}_z^2/2$. In this case, we analytically obtain the size for the gap-like structure close to the Γ point as

$$\Delta_E = 2\Delta_p[3\mu/(4\alpha+5\beta)]^{1/2}. \tag{111}$$

Clearly, Δ_E depends not only on the odd-parity pairing strength Δ_p but also on the material-dependent model parameters μ,α and β.

Moreover, surface states emerge when the chemical potential resides in the range $\mu/E_0 \in [-53.46, 0]$ where $E_0 = 3\Delta_p$, see Figs. 6(a1) and 6(b1). The surface states are visible as long as the A_{2u} channel dominates over the A_{1g} channel [20]. Note that we also observe the superconducting energy gap at the Fermi energy in Fig. 6(b1). It originates from the isotropic intraband pairing in the A_{1g} channel.

The effects of interband pairing in other directions, where momentum is conserved, are depicted in Figs. 6(a2) and 6(b2). For the pure A_{2u} state ($\Delta_s = 0$ and $\Delta_p \neq 0$), the size for the interband pairing becomes maximal at the Γ point and is analytically given by Eq. (111). It decreases monotonically at larger momenta. For the mixed-parity paring state $A_{1g} + A_{2u}$, the surface states are slightly shifted upward due to intraband pairing in the A_{1g} channel, compare Figs. 6(a3) and 6(b3). They also exhibit a weak hybridization with the bulk states at large momenta, depicted in Figs. 6(b2) and 6(b3).

To estimate the magnitude of Δ_p in weakly hole-doped YPdBi, we assume that it is of similar magnitude as for LuPdBi, where it is of the order $\Delta_p = 50 - 300$ ÅμeV [10]. This is because of similarities in the normal-state band structure, point group symmetries, and the type of superconducting pairing. Under this assumption, the energy gap size for the interband pairing becomes $\Delta_E \approx 7.7 - 46.2$ μeV. Notably, an energy resolution below 8 μeV at operating temperatures of 10 mK is achievable in state-of-the-art STM and transport experiments in dilution refrigerators [8].

IX. PAIRING MATRICES

In this section, we demonstrate the method for obtaining the pairing matrices in cubic symmetry, given in Table I of the main paper. The cubic pairing matrices with dependency of momenta up to the linear order can be derived through the relation between SO(3) [21–23] and cubic [7, 23–25] symmetries as we elaborate in the following. In addition, in Ref. [26], a general group-theoretical method to derive the symmetry-allowed pairing matrices for any local degrees of freedom (spin, orbital, and basis site) is introduced. The method relies on the reduction of product representation of the crystallographic point group.

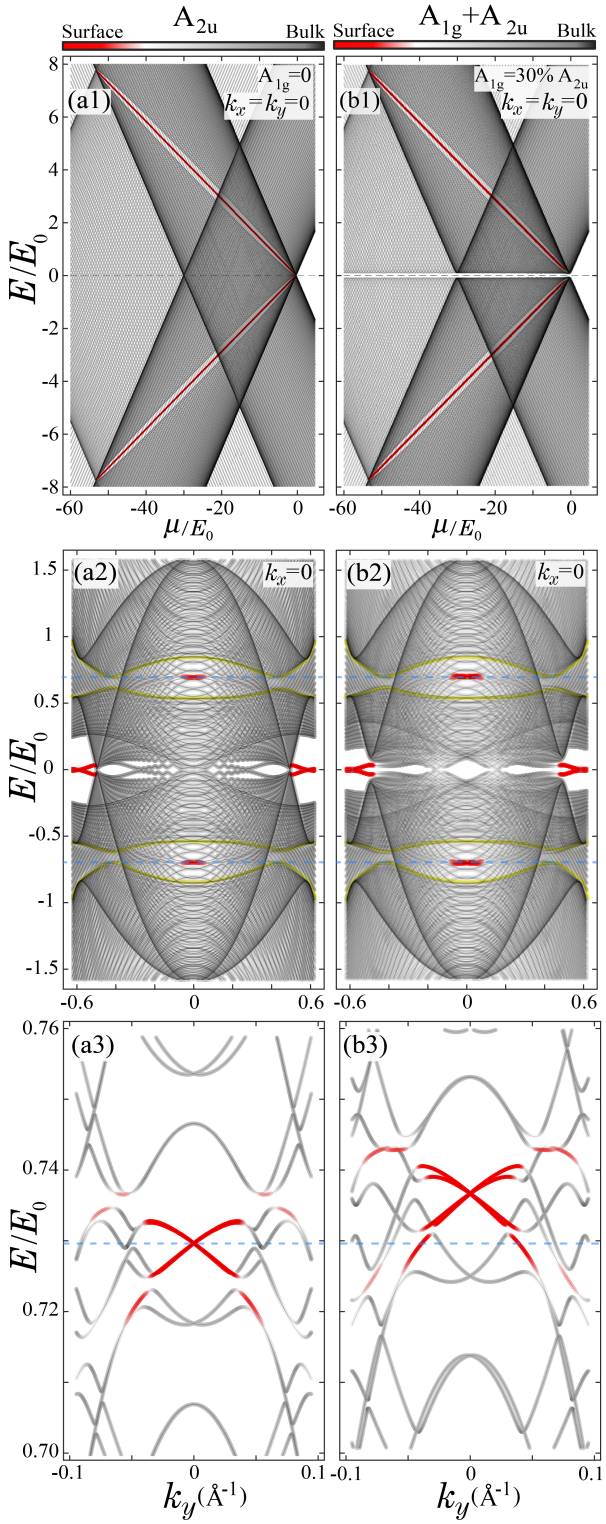

Figure 6. Excitation spectra for (001) slab of hole-doped YPdBi with 160 (layers) obtained by tight-binding regularization of the effective $\mathbf{k}\cdot\mathbf{p}$ model. The superconducting state is $A_{1g} + A_{2u}$ where (a1-a3) $\Delta_s = 0$ and (b1-b3) $\Delta_s = 0.3\Delta_p$. The surface (bulk) states are marked by red (gray) colors. The number of layers in panel (a2,b2) [(a3,b3)] is 200 [360]. The model parameters are the same as those given in Eq. (107). The chemical potential is set to $\mu = -5E_0$ (hole-doped) [20]. Panels (a3) and (b3) are the enlarged view of the regions marked by yellow color in panels (a2) and (b2).

The irreducible representations of SO(3) symmetry are labeled by the total angular momentum J, which combines orbital L and spin S angular momenta. The Cooper pairs formed by two electrons with $j = 3/2$ total angular momentum can have singlet ($J = 0$), triplet ($J = 1$), quintet ($J = 2$), or septet ($J = 3$) angular momenta. Considering orbital angular momentum up to the p-wave channel, i.e., $L \in \{0, 1\}$, the intrinsic spin angular momentum can take values $S \in \{0, 1, 2, 3\}$ according to relation $|L-S| \leq J \leq |L+S|$. The correspondence between the components of a cubic irrep and the SO(3) symmetry is given by the relation [27],

$$\hat{\eta} = \sum_{m_{j_1}, m_{j_2}} \sum_{m_J} [(\hat{\mathcal{O}}_\eta(\hat{J})\hat{\mathcal{R}})_{m_{j_1}, m_{j_2}} \langle J, m_J | m_{j_1}, m_{j_2} \rangle] \hat{\mathcal{N}}_{J,m_J}, \tag{112}$$

where $\langle J, m_J | m_{j_1}, m_{j_2} \rangle$ are the Clebsch-Gordan coefficients, $m_{j_1}, m_{j_2} \in \{\pm 3/2, \pm 1/2\}$, $\hat{\mathcal{R}} = e^{i\pi \hat{J}_y}$, $\hat{\mathcal{N}}_{J,m_J}$ denotes the multipole matrix for the total angular momentum labeled with magnetic quantum number $m_J \in \{-J, \ldots, J\}$, and $\hat{\eta}$ is the matrix representation for the component of an irrep with the normalized basis matrix $\hat{\mathcal{O}}_\eta(\hat{J})$ given in the third and fourth columns of Table II, respectively. Note that the fifth column of Table II is obtained according to Eq. (112). The explicit matrix form of $\hat{\mathcal{N}}_{J,m}$ can be derived by the expansion

$$\hat{\mathcal{N}}_{J,m} = \sum_{m_L, m_S} \langle m_L, m_S | J, m_J \rangle Y^L_{m_L}(\mathbf{k}) \hat{\mathcal{S}}^S_{m_S}, \tag{113}$$

where $\langle m_L, m_S | J, m_J \rangle$ denotes the Clebsch-Gordan coefficient, $Y^L_{m_L}(\mathbf{k})$ and $\hat{\mathcal{S}}^S_{m_S}$ are spherical harmonics and irreducible spin tensor matrices labeled with $m_L \in [-L, \ldots, L]$ and $m_S \in [-S, \ldots, S]$ as the orbital axial angular momentum and spin magnetic quantum number, respectively. Since we are interested in the odd-parity pairings up to linear momenta, the orbital angular momentum is $L = 1$ (p-wave) with the relative spherical harmonics $Y_{1,\pm1}(\mathbf{k}) = \mp\sqrt{3/8\pi} k_\pm/|\mathbf{k}|$ and $Y_{1,0}(\mathbf{k}) = \sqrt{3/4\pi} k_z/|\mathbf{k}|$. Moreover, the derivation method for obtaining $\hat{\mathcal{S}}^S_{m_S}$ follows Refs. [7, 19, 24]. Using the fifth columns of Table II and Eq. (113), the cubic pairing matrices can be derived straightforwardly, giving

$$\hat{\Delta}_{\mathbf{k}} = |\mathbf{k}|\, \hat{\eta}\, \hat{\mathcal{R}}. \tag{114}$$

We start with the A_{2u} irrep to find its pairing matrix. A_{2u} is a one-dimensional irrep appearing only for the $J = 3$ irrep corresponding to $L = 1$ and $S = 3$. The matrix representation for A_{2u} is given by

$$\begin{aligned}\hat{A}_{2u} =& \frac{i}{\sqrt{2}}(\hat{\mathcal{N}}_{2,-2} - \hat{\mathcal{N}}_{2,2}) = \frac{\sqrt{2}}{12i}[Y^1_1(3\hat{\mathcal{S}}^3_{-3} - \sqrt{15}\hat{\mathcal{S}}^3_1) \\ &+\sqrt{12}Y^1_0(\hat{\mathcal{S}}^3_{-2} + \hat{\mathcal{S}}^3_2) + Y^1_{-1}(3\hat{\mathcal{S}}^3_3 - \sqrt{15}\hat{\mathcal{S}}^3_{-1})],\end{aligned} \tag{115}$$

where we dropped the momentum dependency of spherical harmonics. Spin multipole matrices, which fulfill the relation $\hat{\mathcal{S}}^S_{-m_S} = (-1)^{m_S}(\hat{\mathcal{S}}^S_{m_S})^T$, are given by

$$\hat{\mathcal{S}}^3_0 = \frac{\sqrt{5}}{10}\begin{pmatrix} 1 & 0 & 0 & 0 \\ 0 & -3 & 0 & 0 \\ 0 & 0 & 3 & 0 \\ 0 & 0 & 0 & -1 \end{pmatrix}, \hat{\mathcal{S}}^3_1 = \frac{\sqrt{5}}{5}\begin{pmatrix} 0 & -1 & 0 & 0 \\ 0 & 0 & \sqrt{3} & 0 \\ 0 & 0 & 0 & -1 \\ 0 & 0 & 0 & 0 \end{pmatrix}, \tag{116}$$

and

$$\hat{\mathcal{S}}^3_2 = \frac{\sqrt{2}}{2}\begin{pmatrix} 0 & 0 & 1 & 0 \\ 0 & 0 & 0 & -1 \\ 0 & 0 & 0 & 0 \\ 0 & 0 & 0 & 0 \end{pmatrix}, \hat{\mathcal{S}}^3_3 = \begin{pmatrix} 0 & 0 & 0 & -1 \\ 0 & 0 & 0 & 0 \\ 0 & 0 & 0 & 0 \\ 0 & 0 & 0 & 0 \end{pmatrix}. \tag{117}$$

Eventually, the pairing matrix for the A_{2u} irrep takes the form [28]

$$\begin{aligned}\hat{\Delta}_{\mathbf{k}} &= |\mathbf{k}|\, \hat{A}_{2u}\, \hat{\mathcal{R}} \\ &= \Delta \begin{pmatrix} \frac{3}{4}k_- & \frac{\sqrt{3}}{2}k_z & \frac{\sqrt{3}}{4}k_+ & 0 \\ \frac{\sqrt{3}}{2}k_z & \frac{3}{4}k_+ & 0 & -\frac{\sqrt{3}}{4}k_- \\ \frac{\sqrt{3}}{4}k_+ & 0 & -\frac{3}{4}k_- & \frac{\sqrt{3}}{2}k_z \\ 0 & -\frac{\sqrt{3}}{4}k_- & \frac{\sqrt{3}}{2}k_z & -\frac{3}{4}k_+ \end{pmatrix}.\end{aligned} \tag{118}$$

In the next step, we consider the three-dimensional T_{2u} irrep. It appears for the $J = 3$ and $J = 5$ irreps. Due the the nature of $j = 3/2$ electron, only the septet component is allowed. In this case, the first component of the T_{2u} irrep up to linear order of momenta takes the form

$$\begin{aligned}\hat{T}^{(1)}_{2u} =& \frac{1}{\sqrt{2}}(\hat{\mathcal{N}}_{3,-2} + \hat{\mathcal{N}}_{3,2}) = \frac{1}{6\sqrt{2}}[Y^1_{-1}(\sqrt{15}\hat{\mathcal{S}}^3_{-1} + 3\hat{\mathcal{S}}^3_3) \\ &+\sqrt{12}Y^1_0(\hat{\mathcal{S}}^3_2 - \hat{\mathcal{S}}^3_{-2}) - Y^1_1(3\hat{\mathcal{S}}^3_{-3} + \sqrt{15}\hat{\mathcal{S}}^3_1)].\end{aligned} \tag{119}$$

The second component is

$$\begin{aligned}\hat{T}^{(2)}_{2u} =& \frac{1}{4}[\sqrt{3}(\hat{\mathcal{N}}_{3,3} - \hat{\mathcal{N}}_{3,-3}) + \sqrt{5}(\hat{\mathcal{N}}_{3,1} - \hat{\mathcal{N}}_{3,-1})] \\ =& \frac{1}{24}[\sqrt{3}Y^1_{-1}((5\hat{\mathcal{S}}^3_2 - 3\hat{\mathcal{S}}^3_{-2}) - \sqrt{30}\hat{\mathcal{S}}^3_0) \\ &+ \sqrt{3}Y^1_1((5\hat{\mathcal{S}}^3_{-2} - 3\hat{\mathcal{S}}^3_2) - \sqrt{30}\hat{\mathcal{S}}^3_0) \\ &+ Y^1_0(9(\hat{\mathcal{S}}^3_{-3} + \hat{\mathcal{S}}^3_3) + \sqrt{15}(\hat{\mathcal{S}}^3_{-1} + \hat{\mathcal{S}}^3_1))],\end{aligned} \tag{120}$$

and the third component

$$\begin{aligned}\hat{T}^{(3)}_{2u} =& \frac{1}{4i}[\sqrt{3}(\hat{\mathcal{N}}_{3,3} + \hat{\mathcal{N}}_{3,-3}) - \sqrt{5}(\hat{\mathcal{N}}_{3,1} + \hat{\mathcal{N}}_{3,-1})] \\ =& \frac{i}{24}(\sqrt{3}Y^1_1(3\hat{\mathcal{S}}^3_2 - 5\hat{\mathcal{S}}^3_{-2} - \sqrt{30}\hat{\mathcal{S}}^3_0) \\ &+ \sqrt{3}Y^1_{-1}(5\hat{\mathcal{S}}^3_2 - 3\hat{\mathcal{S}}^3_{-2} + \sqrt{30}\hat{\mathcal{S}}^3_0) \\ &+ Y^1_0(9(\hat{\mathcal{S}}^3_{-3} - \hat{\mathcal{S}}^3_3) + \sqrt{15}(\hat{\mathcal{S}}^3_1 - \hat{\mathcal{S}}^3_{-1}))).\end{aligned} \tag{121}$$

Finally, the explicit pairing matrices for the T_{2u} irrep

become

$$\hat{\Delta}_{\mathbf{k}} = |\mathbf{k}|\,\hat{T}^{(1)}_{2u}\,\hat{\mathcal{R}} = \Delta\begin{pmatrix} \frac{3}{4}k_- & \frac{\sqrt{3}}{2}k_z & \frac{\sqrt{3}}{4}k_+ & 0 \\ \frac{\sqrt{3}}{2}k_z & \frac{3}{4}k_+ & 0 & \frac{1}{4}\sqrt{3}k_- \\ \frac{\sqrt{3}}{4}k_+ & 0 & \frac{3}{4}k_- & -\frac{\sqrt{3}}{2}k_z \\ 0 & \frac{\sqrt{3}}{4}k_- & -\frac{\sqrt{3}}{2}k_z & \frac{3}{4}k_+ \end{pmatrix}, \tag{122}$$

$$\hat{\Delta}_{\mathbf{k}} = |\mathbf{k}|\,\hat{T}^{(2)}_{2u}\,\hat{\mathcal{R}} = \Delta\begin{pmatrix} 3k_z & \frac{1}{\sqrt{3}}k'_- & \frac{1}{\sqrt{3}}k_z & ik_y \\ \frac{1}{\sqrt{3}}k'_+ & k_z & 3ik_y & \frac{1}{\sqrt{3}}k_z \\ \frac{1}{\sqrt{3}}k_z & 3ik_y & k_z & \frac{-1}{\sqrt{3}}k'_+ \\ ik_y & \frac{1}{\sqrt{3}}k_z & \frac{-1}{\sqrt{3}}k'_+ & 3k_z \end{pmatrix}, \tag{123}$$

$$\hat{\Delta}_{\mathbf{k}} = |\mathbf{k}|\,\hat{T}^{(3)}_{2u}\,\hat{\mathcal{R}} = \Delta\begin{pmatrix} 3k_z & \frac{-1}{\sqrt{3}}k''_- & \frac{-1}{\sqrt{3}}k_z & -k_x \\ \frac{-1}{\sqrt{3}}k''_- & -k_z & -3k_x & \frac{1}{\sqrt{3}}k_z \\ \frac{-1}{\sqrt{3}}k_z & -3k_x & k_z & \frac{-1}{\sqrt{3}}k''_+ \\ -k_x & \frac{1}{\sqrt{3}}k_z & \frac{-1}{\sqrt{3}}k''_+ & -3k_z \end{pmatrix}, \tag{124}$$

where $k'_\pm = 4k_x \pm ik_y$ and $k''_\pm = k_x \pm 4ik_y$.

E_u (T_{2u}) is a two- (three-) dimensional irrep. It appears for the $J = 2$ and $J = 4$ irreps. In the $j = 3/2$ representation, only the $J = 2$ channel is allowed. Note that the second component of E_u and all the components of T_{2u} can undergo TPTs at FEs. Thus, the expansion for $\hat{E}^{(2)}_u$ is

$$\hat{E}^{(2)}_u = \frac{1}{\sqrt{2}}(\hat{\mathcal{N}}_{2,-2} + \hat{\mathcal{N}}_{2,2}) = \frac{\sqrt{14}}{42}[\sqrt{3}Y^1_1(\sqrt{15}\hat{\mathcal{S}}^3_{-3} + \hat{\mathcal{S}}^3_1) + \sqrt{3}Y^1_{-1}(\hat{\mathcal{S}}^3_{-1} + \sqrt{15}\hat{\mathcal{S}}^3_3) - \sqrt{15}Y^1_0(\hat{\mathcal{S}}^3_{-2} + \hat{\mathcal{S}}^3_2)]. \tag{125}$$

The pairing matrix for $E^{(2)}_u$ becomes

$$\hat{\Delta}_{\mathbf{k}} = |\mathbf{k}|\,\hat{E}^{(2)}_u\,\hat{\mathcal{R}} = \Delta\begin{pmatrix} 5\sqrt{3}k_- & -5k_z & -k_+ & 0 \\ -5k_z & -\sqrt{3}k_+ & 0 & k_- \\ -k_+ & 0 & \sqrt{3}k_- & -5k_z \\ 0 & k_- & -5k_z & -5\sqrt{3}k_+ \end{pmatrix}. \tag{126}$$

Likewise, the pairing matrix for the first component of the T_{2u} irrep can be straightforwardly derived

$$\hat{\Delta}_{\mathbf{k}} = |\mathbf{k}|\,\hat{T}^{(1)}_{2u}\,\hat{\mathcal{R}} = \Delta\begin{pmatrix} -5\sqrt{3}k_- & 5k_z & k_+ & 0 \\ 5k_z & \sqrt{3}k_+ & 0 & k_- \\ k_+ & 0 & \sqrt{3}k_- & -5k_z \\ 0 & k_- & -5k_z & -5\sqrt{3}k_+ \end{pmatrix}, \tag{127}$$

and the second component takes the form

$$\hat{\Delta}_{\mathbf{k}} = |\mathbf{k}|\,\hat{T}^{(2)}_{2u}\,\hat{\mathcal{R}} = \Delta\begin{pmatrix} 0 & -5k_- & 4k_z & \sqrt{3}k_x \\ -5k_- & 4\sqrt{3}k_z & 3\sqrt{3}k_x & -4k_z \\ 4k_z & 3\sqrt{3}k_x & -4\sqrt{3}k_z & -5k_+ \\ \sqrt{3}k_x & -4k_z & -5k_+ & 0 \end{pmatrix}. \tag{128}$$

Finally, the pairing potential for the third component of T_{2u} becomes

$$\hat{\Delta}_{\mathbf{k}} = |\mathbf{k}|\,\hat{T}^{(3)}_{2u}\,\hat{\mathcal{R}} = \Delta\begin{pmatrix} 0 & -5k_- & 4k_z & i\sqrt{3}k_y \\ -5k_- & 4\sqrt{3}k_z & 3i\sqrt{3}k_y & 4k_z \\ 4k_z & 3i\sqrt{3}k_y & 4\sqrt{3}k_z & 5k_+ \\ i\sqrt{3}k_y & 4k_z & 5k_+ & 0 \end{pmatrix}. \tag{129}$$

To sum up, the relation between cubic point group symmetry and full SO(3) symmetry enabled us to explicitly obtain the cubic pairing matrices. This method can also be applied to other point group symmetries.

* masoud.bahari@physik.uni-wuerzburg.de

[1] D. F. Agterberg, P. M. R. Brydon, and C. Timm, Phys. Rev. Lett. **118**, 127001 (2017).

[2] A. P. Schnyder, S. Ryu, A. Furusaki, and A. W. W. Ludwig, Phys. Rev. B. **78**, 195125 (2008).

[3] T. Morimoto and A. Furusaki, Phys. Rev. B **88**, 125129 (2013).

[4] C.-K. Chiu, J. C. Y. Teo, A. P. Schnyder, and S. Ryu, Rev. Mod. Phys. **88**, 035005 (2016).

[5] L. Fu and C. L. Kane, Phys. Rev. B **76**, 045302 (2007).

[6] T. L. Hughes, E. Prodan, and B. A. Bernevig, Phys. Rev. B **83**, 245132 (2011).

[7] J. W. F. Venderbos, L. Savary, J. Ruhman, P. A. Lee, and L. Fu, Phys. Rev. X. **8**, 011029 (2018).

[8] J. Schwenk, S. Kim, J. Berwanger, F. Ghahari, D. Walkup, M. R. Slot, S. T. Le, W. G. Cullen, S. R. Blankenship, S. Vranjkovic, H. J. Hug, Y. Kuk, F. J. Giessibl, and J. A. Stroscio, Review of Scientific Instruments **91**, 071101 (2020).

[9] Y. Nakajima, R. Hu, K. Kirshenbaum, A. Hughes, P. Syers, X. Wang, K. Wang, R. Wang, S. R. Saha, D. Pratt, J. W. Lynn, and J. Paglione, Sci. Adv. **1**, 10.1126/sciadv.1500242 (2015).

[10] K. Ishihara, T. Takenaka, Y. Miao, Y. Mizukami, K. Hashimoto, M. Yamashita, M. Konczykowski, R. Masuki, M. Hirayama, T. Nomoto, R. Arita, O. Pavlosiuk, P. Wiśniewski, D. Kaczorowski, and T. Shibauchi, Phys. Rev. X. **11**, 041048 (2021).

[11] P. Rüßmann, M. Bahari, S. Blügel, and B. Trauzettel, Phys. Rev. Res. **5**, 043181 (2023).

[12] P. Rüßmann, D. Antognini Silva, D. S. G. Bauer, P. Baumeister, P. F. Bornemann, J. Bouaziz, S. Brinker, J. Chico, P. H. Dederichs, B. H. Drittler, F. Dos Santos, M. dos Santos Dias, N. Essing, G. Geranton, I. Klepetsanis, A. Kosma, N. H. Long, S. Lounis, P. Mavropoulos,

E. Mendive Tapia, C. Oran, N. Papanikolaou, E. Rabel, B. Schweflinghaus, N. Stefanou, A. R. Thiess, R. Zeller, B. Zimmermann, and S. Blügel, Judftteam/jukkr: v3.6 (2022).
[13] P. Rüßmann and S. Blügel, Phys. Rev. B **105**, 125143 (2022).
[14] A. Jain, S. P. Ong, G. Hautier, W. Chen, W. D. Richards, S. Dacek, S. Cholia, D. Gunter, D. Skinner, G. Ceder, and K. A. Persson, APL Materials **1**, 011002 (2013).
[15] Data retrieved from the Materials Project for YBiPd (mp-1008624) from database version v2023.11.1.
[16] V. Bhardwaj, A. Bhattacharya, S. Srivastava, V. V. Khovaylo, J. Sannigrahi, N. Banerjee, B. K. Mani, and R. Chatterjee, Sci. Rep. **11**, 7535 (2021).
[17] W. L. Vosko, S. H. and N. M., Can. J. Phys. **58**, 10.1139/p80-159 (1980).
[18] W. Yang, T. Xiang, and C. Wu, Phys. Rev. B. **96**, 144514 (2017).
[19] M. Bahari, S.-B. Zhang, and B. Trauzettel, Phys. Rev. Research **4**, L012017 (2022).
[20] In Fig. (6), we have enlarged Δ_p by a factor 3 as compared to normal state energy scales for illustration reasons. Otherwise, finite size effects are destructive for the emergence of the surface states at finite excitation energies.
[21] W. Yang, Y. Li, and C. Wu, Phys. Rev. Lett. **117**, 075301 (2016).
[22] C. Fang, B. A. Bernevig, and M. J. Gilbert, Phys. Rev. B **91**, 165421 (2015).
[23] L. Savary, J. Ruhman, J. W. F. Venderbos, L. Fu, and P. A. Lee, Phys. Rev. B. **96**, 214514 (2017).
[24] J. Yu and C.-X. Liu, Phys. Rev. B. **98**, 104514 (2018).
[25] T. Kawakami, T. Okamura, S. Kobayashi, and M. Sato, Phys. Rev. X **8**, 041026 (2018).
[26] C. Timm and A. Bhattacharya, Phys. Rev. B. **104**, 094529 (2021).
[27] S.-T. Tamura, S. Iimura, and S. Hoshino, Phys. Rev. B **102**, 024505 (2020).
[28] P. M. R. Brydon, L. Wang, M. Weinert, and D. F. Agterberg, Phys. Rev. Lett. **116**, 177001 (2016).